Plasma Exosomes in Insulin Resistant Obesity Exacerbate Progression of Triple Negative Breast Cancer

Pablo Llevenes[1], Andrew Chen[2,3], Matthew Lawton, Yuhan Qiu[1], Michael Seen[1], Stefano Monti[2,3], and Gerald V. Denis[1,2,4]

[1]Cancer Center, Boston University Chobanian and Avedisian School of Medicine, Boston, Massachusetts

[2]Department of Medicine, Computational Biomedicine Section, Boston University Chobanian and Avedisian School of Medicine, Boston, MA, 02118, USA

[3]Bioinformatics Program, Boston University, Boston, MA, 02215, USA

[4]Department of Pharmacology and Experimental Therapeutics, Boston University Chobanian and Avedisian School of Medicine, Boston, Massachusetts

Running Title. Exosomes drive metastasis of TNBC in obesity

Keywords. breast cancer, triple-negative, metastasis, breast cancer migration, exosome

Grant Support. This work was supported by grants from NIH: U01CA182898, U01CA243004 and R01CA222170 to G.V. Denis.

Corresponding Author. Gerald V Denis, Boston University School of Medicine, 72 East Concord Street, Rm K408, Boston, MA 02118 Phone: 617-414-1371, Lab: 617-414-1372, Fax 617-638-5673; E-mail: gdenis@bu.edu

Conflict of interest. The authors affirm that they have no conflicts to disclose.

Abstract word count: 206

Word count, excluding figure legends and references: 6,334

Main Text Figures: 7

Supplementary Figures: 5

Supplementary Tables: 1

References: 46

Abstract

Breast cancer, the most common cancer among women worldwide, continues to pose significant public health challenges. Among the subtypes of breast cancer, triple-negative breast cancer (TNBC) is particularly aggressive and difficult to treat due to the absence of receptors for estrogen, progesterone, or human epidermal growth factor receptor 2, rendering TNBC refractory to conventional targeted therapies. Emerging research underscores the exacerbating role of metabolic disorders, such as type 2 diabetes and obesity, on TNBC aggressiveness. Here, we investigate the critical cellular and molecular factors underlying this link. We explore the pivotal role of circulating plasma exosomes in modulating the tumor microenvironment and enhancing TNBC aggressiveness. We find that plasma exosomes from diet-induced obesity mice induce epithelial-mesenchymal transition features in TNBC cells, leading to increased migration *in vitro* and enhanced metastasis *in vivo*. We build on our previous reports demonstrating that plasma exosomes from obese, diabetic patients, and exosomes from insulin-resistant 3T3-L1 adipocytes, upregulate key transcriptional signatures of epithelial-mesenchymal transition in breast cancer. Bioinformatic analysis reveals that TNBC cells exhibit higher expression and activation of proteins related to the Rho-GTPase cascade, particularly the small Ras-related protein Rac1. Our approach suggests novel therapeutic targets and exosomal biomarkers, ultimately to improve prognosis for TNBC patients with co-morbid metabolic disorders.

206 words

Breast cancer is the most common cancer among women worldwide and represents a major public health concern due to its high incidence and significant mortality rates. In the United States alone, approximately 297,790 new cases of invasive breast cancer were reported in women in 2023, resulting in an estimated 43,700 deaths. Additionally, around 310,720 new cases of invasive breast cancer and about 56,500 new cases of ductal carcinoma in situ are expected to be diagnosed in women in 2024, with an estimated 42,250 deaths resulting from the disease (1).

Among the various subtypes of breast cancer, triple-negative breast cancer (TNBC) stands out due to its aggressive nature and poor prognosis. TNBC is characterized by the absence of three critical receptors: estrogen receptor (ER), progesterone receptor, and human epidermal growth factor receptor 2 (HER2), which are common targets for breast cancer therapies (2). Consequently, TNBC lacks targeted treatment options, relying primarily on conventional cytotoxic therapies. This limitation contributes to the subtype's high recurrence rates and significantly lower survival rates compared to other forms of breast cancer (3). While other types of invasive breast cancer, such as localized ER-positive and HER2-positive, have a 5-year relative survival rate of around 99% and 93%, respectively, the 5-year relative survival rate for TNBC is approximately 91%. However, this rate drops dramatically to about 12% for distant metastases (4). This stark decrease underscores the urgent need for more effective treatment strategies for metastatic TNBC.

Recent years have seen a growing interest in the intersection of TNBC with metabolic disorders, such as type 2 diabetes (T2D) and obesity, as these conditions are linked to heightened cancer aggressiveness and poorer patient outcomes (5). Obesity, as a chronic inflammatory condition, disrupts tissue insulin sensitivity and function, leading to the development of T2D and adipocyte insulin resistance (IR) (6). This systemic inflammation causes metabolic abnormalities that release various pro-inflammatory factors, such as cytokines interleukin (IL)-6, tumor necrosis factor (TNF)-α, and leptin, into the plasma (7,8). The inflammatory milieu created by obesity promotes cancer development and progression through the interactions of these circulating factors with the tumor and its microenvironment (9,10).

Emerging research has increasingly focused on the role of exosomes in cancer aggressiveness. Exosomes are small extracellular vesicles (~100nm) found in blood and other fluids, containing proteins, lipids, and nucleic acids that reflect the content of their cells of origin. These vesicles facilitate intercellular communication and can reprogram recipient cells (11). Depending on the metabolic state of the originating cell, exosomes can create a synergistic environment that promotes processes in malignant cells, such as epithelial-to-mesenchymal transition (EMT) and cancer stem cell (CSC) formation, thereby contributing to a more aggressive tumor phenotype (12,13).

Our research builds upon this foundation by exploring a novel aspect of the interaction between metabolic disorders and TNBC aggressiveness. Our preliminary studies have demonstrated that exosomes from IR adipocytes promote significant EMT and tumor progression in breast cancer models, compared to insulin-sensitive controls (14). We have also observed that exosomes from T2D patient plasma contain miRNAs that enhance tumor cell invasiveness and metastatic potential compared to non-diabetic controls (15,16). Given the substantial impact of metabolic diseases on TNBC outcomes, our research aims to delve deeper into the molecular mechanisms underlying this interaction.

We hypothesize that exosomes derived from adipocytes and plasma play a pivotal role in modulating the tumor microenvironment to favor tumor aggressiveness and metastasis. We used murine models in our approach to test this hypothesis. Exosomes from adipocytes and plasma of mice maintained on a high-fat diet (HFD) for 12 weeks carry unique biomolecules that dramatically alter the behavior of TNBC cells, promoting processes such as EMT and enhanced metastatic potential, unlike matched exosomes from low-fat diet (LFD) controls. Our study offers a novel contribution by investigating the functional impact of these exosomes across different metabolic states, with the goal of identifying new therapeutic targets and biomarkers. This research has the potential to reveal previously unrecognized mechanisms by which metabolic dysregulation drives TNBC progression, ultimately informing more effective strategies for managing this aggressive breast cancer subtype in patients with co-morbid metabolic disorders.

Materials and Methods

Cell culture

Murine E0771-GFP cells as a syngeneic TNBC model for C57BL/6J mice were a gift of Dr. Timothy Padera. The cells were cultured in DMEM medium with 4.5 g/L glucose and L-glutamine, without sodium pyruvate, supplemented with 10% fetal bovine serum (FBS), 100 units/mL penicillin and 10 μg/mL streptomycin (Corning), and incubated at 37°C with 100% humidity and 5% CO_2. Cell lines were tested monthly for mycoplasma using a Mycoplasma Detection Kit (Invivogen) and used within 10 passages.

Animals

Six-week-old female C57BL/6J mice were obtained from Jackson Laboratory and acclimated at the Boston University Animal Facility for one week. Mice were fed *ad libitum* a lard-based high-fat diet (HFD, 60% of calories from fat, Research Diets D12492i) or a matched low-fat diet (LFD, 10% fat, Research Diets D12450Ji) for 12 weeks, ensuring obesity in the HFD group. All animal experiments followed the approved procedures of the Institutional Animal Care and Use Committee (IACUC) of Boston University Medical Center. For all consequent experiments, E0771-GFP cells were treated with exosomes on Day 0 and allowed to proliferate for 72 hours up to a confluence of 70%.

Glucose tolerance test, insulin tolerance tests, weight curves and body mass index

Glucose tolerance tests (GTTs) and insulin tolerance tests (ITTs) were performed on adult female mice (18 weeks old, with 12 weeks on diet: N = 5 HFD and 5 matching control LFD). For GTT, after a 6-hour fast, mice were administered a glucose solution via oral gavage at a dose of 2 g/kg body weight. Blood glucose levels were measured at baseline (time = 0) and at 15, 30, 60, and 120 minutes post-glucose administration using a glucometer (Abbott, AlphaTrak2) with blood samples collected from the tail vein. For ITT, human recombinant insulin (Gibco; 0.75 U/kg body weight) from a stock solution of 4 mg/mL was administered intraperitoneally after a 6-hour fast. Blood was collected from the tail vein immediately before insulin injection (time = 0) and at

15, 30, 60, and 120 minutes after injection. Blood glucose levels were then plotted to generate glucose and insulin tolerance curves, and the area under the curve (AUC) was calculated to compare glucose and insulin tolerance between the obese and control groups. Throughout the tests, mice were observed for any signs of hypoglycemia or adverse reactions.

The weight of the mice was measured weekly for both the HFD and LFD groups throughout the 12-week diet period. At the end of the 12 weeks, body mass index (BMI) was calculated to confirm the obese status of the HFD group compared to the LFD group. BMI was determined using the formula: BMI = weight (g) / length (cm)^2. This calculation ensured an accurate assessment of obesity status in the HFD group relative to the control LFD group.

Isolation of primary adipocytes and blood plasma from mouse

After completing the 12-week diet, mice were euthanized, and their visceral adipose tissue depots (perigonadal) were excised. The tissue was minced in cold phosphate buffered saline (PBS) pH 7.4 in a tissue culture dish and filtered through a 250-micron mesh. The minced tissue was then transferred to a 50 mL Falcon tube containing liberase (Sigma Aldrich) digestion buffer (10 mg liberase, 300 μL dH_2O, 500 μL of 1M HEPES, pH 7.4) in a total volume of 10 mL Dulbecco's Modified Eagle Medium (DMEM) without fetal bovine serum (FBS). Tubes were placed in a shaker at 37°C, with oscillation at 120 revolutions per minute (RPM) for at least one hour. The duration of shaking was adjusted based on the initial size of the depot to ensure thorough digestion. After digestion, the mixture was filtered through a 250-micron mesh and transferred to a new tube. To neutralize the digestion, 5 mL of FBS was added. The sample was then centrifuged at 500 rcf for 5 minutes, followed by vigorous shaking and another centrifugation at 500 rcf for 5 minutes at room temperature. The layer of lipid-laden adipocytes floating at the top of the suspension was isolated and placed in 10 mL of complete DMEM in a 10 cm dish and incubated at 37°C for 24 hours to allow the exosome release into the media for collection.

Retro-orbital blood extraction was performed using capillary and collection tubes, both treated with EDTA to prevent coagulation. The initial blood volume collected after opening the wound was discarded and blood samples were kept at room temperature for less than one hour. The collected blood was first centrifuged at 250 rcf for 25 minutes at room temperature. The supernatant (plasma) was then carefully transferred to a new tube and centrifuged at 2,500 rcf for 20 minutes. The resulting plasma was collected, and the pellet was discarded. Plasma samples were stored at -80°C until further exosome purification.

Exosome purification

Exosomes were either isolated from visceral adipose tissue or mouse plasma. For exosomes isolated from visceral adipose tissue, conditioned media (typically 15 mL) was centrifuged at 300 × g for 10 min in a 15 mL conical tube to remove cells and debris. The supernatant was then transferred to an Amicon Ultra-15 (Millipore-Sigma; REF-UFC910008) 100K centrifugal filter and centrifuged at 3,500 × g for 15 min to reach a final volume of 0.5 ml. Exosomes were then purified by size exclusion chromatography on a qEV Original column, using an automatic fraction collector (AFC, serial number: V1-0395, IZON), as previously described (15). For exosome isolation from plasma, approximately 20 μL of plasma was processed using 35 nm qEVsingle Gen 2 columns. The columns were set with default AFC parameters. The collected fraction contained the exosomes and was diluted 1:100 (exosomes:PBS+EDTA). The size distribution and concentration of exosomes were determined before each biological experiment using the NanoSight NS300 system (Malvern Panalytical). Based on this quantitation, the ratio of exosomes to E0771 cells was 100,000:1 on Day 0 of exposure.

PCR array

Total RNA was extracted from mouse E0771 cells using the RNeasy Plus Mini Kit (Qiagen, 74136). From each sample, 1 μg of RNA was used to prepare 20 μL of cDNA using the QuantiTect Reverse Transcription Kit (Qiagen, 205313). The Mouse RT2 Profiler™ PCR Array for Epithelial to Mesenchymal Transition (EMT) (Qiagen, PAMM-090Z) was utilized for this study. Each cDNA sample (102 μL) was mixed with 1,350 μL of RT2 SYBR Green-ROX qPCR Mastermix (Qiagen, 330522) and 1,248 μL of RNAse-free water. This brought

the total volume to 2,700 µL, which was thoroughly mixed by pipetting. Using an automated pipettor, 25 µL aliquots of the reaction mix were distributed into each well of the array. Real-time PCR was conducted using the StepOne Plus PCR instrument (Applied Biosystems) following the manufacturer's instructions. The results were analyzed and plotted using the RT2 Profiler web-based software provided by Qiagen®.

Ingenuity pathway analysis

To predict disease functions and downstream pathways, data were analyzed using Ingenuity Pathway Analysis (IPA) software (QIAGEN®). Core analysis was first conducted, followed by comparison analysis on all experimental conditions, including replicates. This approach enabled the identification and interpretation of biological pathways, molecular networks, and functional connections relevant to the dataset.

mRNA sequencing and analysis

Total RNA was extracted from the cells using the RNeasy Plus Mini Kit (QIAGEN, Cat. No. 74136) following the manufacturer’s protocol. RNA sequencing data was processed using the nf-core rnaseq pipeline (17), and the resulting expression matrices were filtered to exclude genes with low expression (fewer than 3 reads per million in at least 3 samples) and corrected for library size differences using the DESeq2 package (18). Differential gene expression analysis was then performed using DESeq2 between the Control (for *in vitro* analysis LFD, and for brain metastasis analysis LB plus CB) and HFD experimental groups. To examine the prognostic value of these DEGs in human tumors, survival analysis was conducted using a Cox proportional hazards model and visualized using the survminer package (19) in breast cancer data from both The Cancer Genome Atlas (TCGA) (20) and METABRIC (21). Each Cox model also included patient age and proliferation expression as covariates to estimate prognostic value independent of age and proliferation-related mechanisms (22)

Cell migration assay

Cells were initially treated with exosomes as previously described, then switched from normal medium to serum-free medium for 3 hours. After this period, cells were trypsinized, counted, and 30,000 cells were seeded into the upper wells of 24-well transwell plates (8-μm pore size, Thermo Fisher Scientific®) with 300 μL of serum-free medium. The bottom wells were filled with 500 μL of DMEM media supplemented with 10% FBS to serve as a chemoattractant. The cells were then allowed to migrate for 24 hours. After the migration period, the media was aspirated, and the transwell inserts were gently washed with PBS. The upper side of the membrane was carefully cleaned to remove non-migrated cells using a cotton swab with a gentle swirling motion, taking care not to press too hard to avoid background signals and disruption of the filter monolayer. The migrated cells on the lower side of the membrane were fixed with 500 μL of cold 100% methanol for 10 minutes at -20°C. After fixation, the methanol was aspirated, and inserts were cleaned with PBS. Once the inserts were dry, the cells were stained with 500 μL of 1% crystal violet (w/v) in 2% ethanol (v/v) for 10 minutes at room temperature. The crystal violet solution was then aspirated, and the inserts were washed three times with PBS. The inserts were allowed to air dry for 30 minutes. Images of the stained migrated cells were captured using an EVOS® XL Core digital inverted microscope. The percentage of migration was quantified using ImageJ software (National Institutes of Health, Bethesda, MD).

Cellular symmetry analysis

Cell images were captured using an EVOS XL Core digital inverted microscope. Cell morphological parameters were analyzed using CellProfiler® software (Broad Institute, MA). The perimeter was defined as the total length of the cell's outer boundary. Circularity was calculated using the formula $4\pi \times (\text{area}/\text{perimeter}^2)$ where a value of 1.0 denotes a perfect circle, and values approaching 0.0 indicate decreasing circularity and a more irregular shape.

Proteomics Analysis

Samples stored at -80°C were thawed on ice and lysed using guanidine hydrochloride lysis buffer (6M guanidine hydrochloride, 100mM Tris pH 8.5, 40mM chloroacetamide, 10mM TCEP), followed by vortex mixing, heating at 95°C for 5 minutes, and sonication. Protein concentration was determined via Bradford assay. Samples were diluted to <0.75M guanidine hydrochloride using 100mM Tris-HCl (pH 8.0), digested overnight with trypsin (1:50) at 37°C, and acidified with 1% formic acid. Peptides were desalted, dried, and quantified using the Pierce peptide assay. 100 μg of peptides per sample were labeled with TMTpro, pooled, desalted, and fractionated using reversed-phase HPLC, yielding 48 fractions. For phosphopeptide enrichment, samples were resuspended in 80% acetonitrile/0.5% trifluoroacetic acid and enriched with iron-based beads (Cube Biotech). Phosphopeptides were eluted, dried, and analyzed by mass spectrometry using an Exploris 480 with FAIMS Pro. Peptides were separated by HPLC using a 120-minute gradient and analyzed in positive ion mode. Data acquisition was done in data-dependent mode, selecting the 12 most abundant ions for fragmentation. Phosphopeptides were analyzed similarly with a shorter gradient. Raw spectra were searched against the Uniprot (mus musculus) database using MaxQuant. Reporter ion intensities were normalized using Loess normalization, and data were analyzed with OmicsNotebook. Differential expression was assessed using Limma, with p-values corrected via Benjamini-Hochberg. Functional enrichment analyses were performed using GSEA and EnrichR.

Cell count

The number of cells was determined by counting triplicates for each condition. Cells were trypsinized and stained with a 1:10 trypan blue dilution (trypan blue:PBS) to distinguish viable cells from non-viable cells. The cell count was performed using a hemocytometer (Neubauer Improved) under an EVOS® XL Core digital inverted microscope.

Clonogenic Assay

E0771-GFP cells were trypsinized and resuspended in a cold PBS solution and 100,000 were injected into the second mammary fat pad of 6-week-old C57BL/6J female mice and sacrificed four weeks post-injection. Tissues were homogenized using the previously described digestion buffer containing liberase. The resulting homogenate was filtered through cell strainer filters of 40 µm pore size, ensuring the result was a single cell suspension. Each homogenate was plated separately in 150mm culture dishes and allowed to settle. After settling, the media was gently removed and replaced to eliminate non-adherent cells, and the adherent cells were left to grow for one week to form colonies. The colonies were then analyzed using a Zeiss® Stereo Discovery V12 microscope equipped with filters for detecting GFP positive cells, along with an attached Axiocam MRC camera by Zeiss®. The images were processed using Adobe® Photoshop (Adobe Inc., San Jose, CA, USA) to create a photomerged final image, providing a comprehensive view of the whole plate. The colonies were then counted, and the cell number and the area covered by the cells on the total plate were quantified using ImageJ® software (National Institutes of Health, Bethesda, MD, USA). Primary tumors were carefully excised and measured. The dimensions of each tumor were recorded in three orthogonal directions (length, width, and height) using a digital caliper. Subsequently, the tumors were weighed using an analytical balance to obtain their mass.

Wound healing assay

Cells were seeded for a 3-day exosome treatment in 12-well plates and allowed to reach a confluence of 90%, at which point the surface of each well was scratched using a sterile 10-µL pipette tip. The cells were then incubated overnight with increasing concentrations of the Rac1 inhibitor EHT 1864 (Cat. No. 387210R, Tocris®). EHT 1864 was prepared in a series of concentrations: 5, 10, 20, 25, 30, 40, and 50 µM. The wound closure was monitored and imaged at 0 and 24 hours post-treatment using an EVOS® XL Core digital inverted microscope with a digital camera. The wound closure was measured using ImageJ® software, and the

percentage of wound closure was calculated using the formula: Percentage of Wound Closure = [(Wound Area at 0 hours - Wound Area at 24 hours) / Wound Area at 0 hours] × 100.

Statistical Analyses

Statistical analyses were performed using GraphPad Prism software. Depending on the data distribution, either parametric (Student's t-test or ANOVA) or non-parametric tests (Mann-Whitney or Kruskal-Wallis) were applied as indicated. The following symbols were used to denote the level of statistical significance: ns, $p > 0.05$; *, $p < 0.05$; **, $p < 0.01$; ***, $p < 0.001$; ****, $p<0.0001$. For parametric data, Student's t-tests were used to compare two groups, and ANOVA was used for multiple group comparisons. For non-parametric data, equivalent non-parametric tests such as the Mann-Whitney U test for two groups or the Kruskal-Wallis test for multiple groups were utilized. All results are presented as mean ± standard deviation (SD) unless otherwise indicated.

RESULTS

Establishment of Obesity and Insulin Resistance in HFD Mice

To evaluate the effects of HFD on exosome production, six-week-old female C57BL/6J mice were fed either a lard-based high-fat diet (60% of calories from fat) or a matched low-fat diet (10% of calories from fat). After 12 weeks on diet, the HFD group developed obesity, glucose intolerance and insulin resistance, confirmed by significant weight gain and impaired glucose metabolism, as shown in Fig. 1 (A-G). To confirm the obesity in the model, weekly measurements over 12 weeks demonstrated a statistically significant weight increase (Fig. 1A and B), that was further confirmed by measuring the BMI at the 12th week (Fig. 1C), observing a BMI greater than 4 kg/m^2 (obese) for the HFD group. To confirm the impaired glucose metabolism, oral glucose tolerance tests (oGTT) and insulin tolerance tests (ITT), were carried out (Fig. 1D-G). Showing impaired glucose metabolism in the HFD group compared to LFD. These results confirmed the successful establishment

of the obesity model, evidenced by significant physiological changes, including weight gain, insulin resistance, and impaired glucose metabolism.

After the establishment of obesity and systemic insulin resistance in the HFD group, but not in the LFD group, we proceeded with exosomal extraction. Blood was collected via retro-orbital extraction for plasma-derived exosomes, and visceral perigonadal tissue was harvested for adipocyte-derived exosome isolation. No differences were found in diameter and abundance between LFD and HFD exosomes (Supplementary Fig. S1A-B).

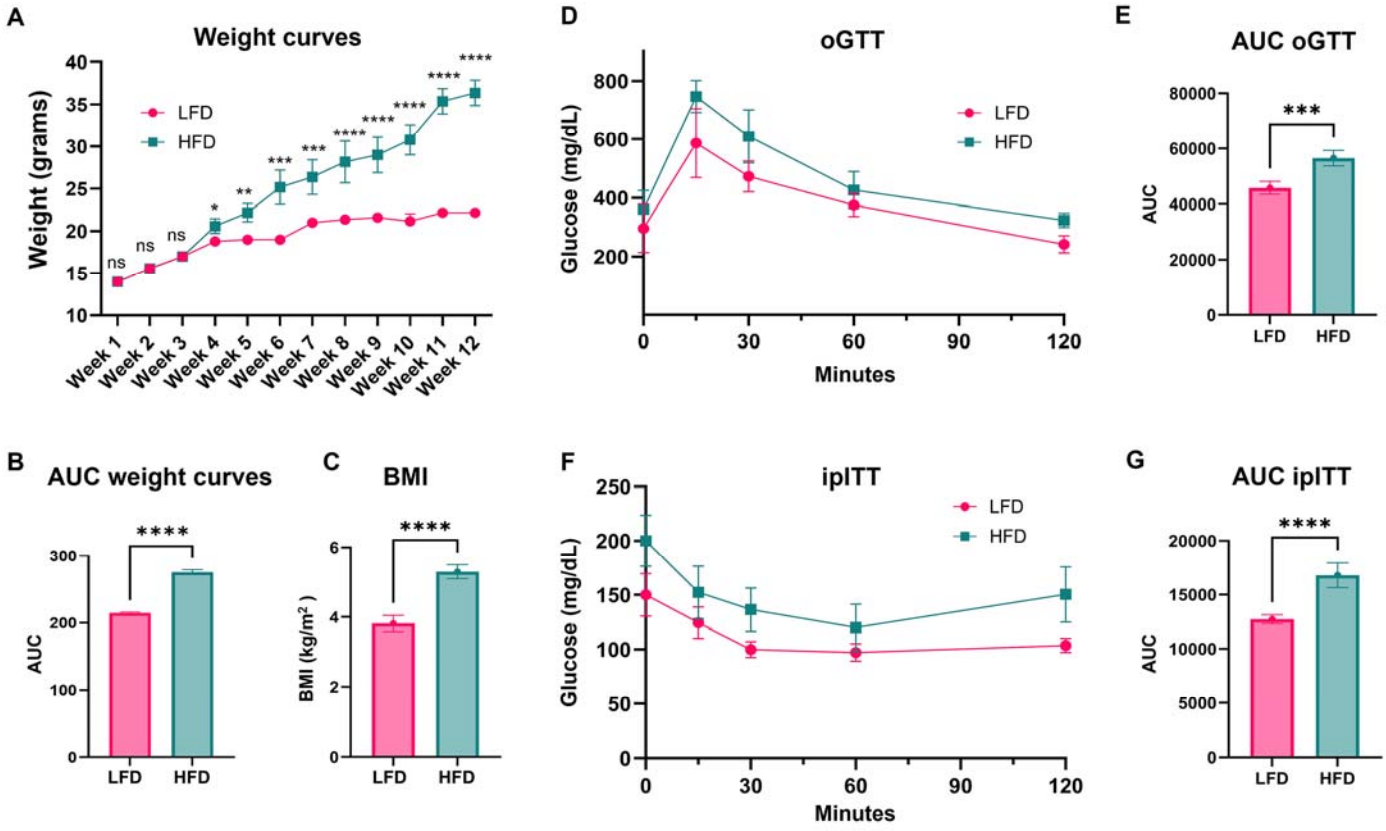

Figure 1. Validation of the obese mouse model.

Measurements were taken after 12 wk of feeding *ad libitum* either HFD or LFD to 6-wk-old female C57BL/6J mice. (A) Weight curves over time. (B) Area under the curve (AUC) analysis of weight. (C) Body mass index (BMI, kg/m²) after 12 wk. (D) oGTT curves. (E) AUC analysis of oGTT. (F) ITT curves. (G) AUC analysis of ITT. LFD, Low-fat diet; HFD, High-fat diet; oGTT, oral glucose tolerance test; ITT, insulin tolerance test. N=5. Data were analyzed by multiple t-tests; statistical significance was ns (not significant), *$p < 0.05$, **$p < 0.01$, ***$p < 0.001$, ****$p < 0.0001$. All data are shown as mean ± SD.

Differential Gene Expression and Morphological Changes Induced by Adipocyte-Derived Exosomes

Using exosomes from visceral fat, an EMT-array revealed differential gene expression after a three-day treatment (Fig. 2A and B) (Supplementary Fig. S2A, S2B). Notably, Snai1 and Ctnnb1 were significantly upregulated in HFD-treated cells compared to LFD-treated cells (Supplementary Fig. S2C), as demonstrated in a volcano plot (Fig. 2C). Enrichment analysis using Ingenuity Pathway Analysis (IPA) software identified the most enriched pathways as those related to cytoskeleton organization, cell survival and movement. These findings were visualized through bubble and bar charts (Fig. 2D). This result prompted further analysis of cell morphology, which revealed increased perimeter and decreased circularity in HFD-treated cells (Fig. 2E). These morphological changes are indicative of cytoskeletal restructuring consistent with a pro-EMT phenotype. Despite these significant molecular and morphological changes, migration assays did not show any differences in migratory capacity between HFD-treated and LFD-treated groups (Fig. 2F). Similarly, cell viability assays revealed no significant differences in cell survival between the two groups (Fig. 2G). These results suggest that while HFD-derived adipocyte exosomes promote molecular and structural changes associated with EMT, additional factors present in plasma exosomes account for migration differences.

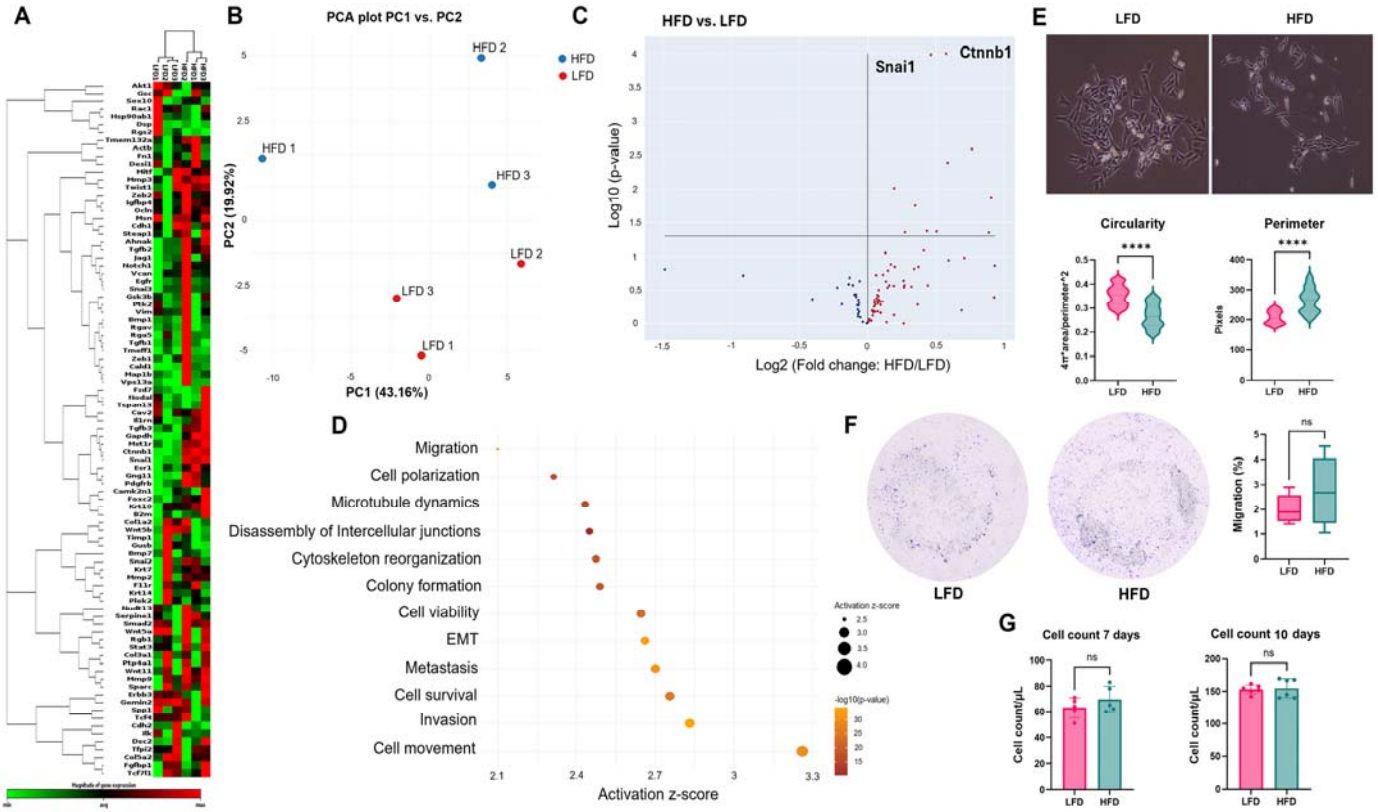

Figure 2. Adipocyte-derived exosomes from HFD-fed mice induce transcription of EMT genes in E0771 cells.

E0771 cells were cultured for 3 days with adipocyte-derived exosomes of either HFD or LFD fed mice. Expression of selected EMT genes was analyzed by commercial PCR array and Ingenuity Pathway Analysis (IPA). (A) Heatmap of EMT genes showing differential expression. (B) Principal Component Analysis (PCA) showing clustering of triplicates of the same group regarding EMT gene expression. (C) Volcano plot of significantly upregulated genes (*e.g.*, *Snai1*, *Ctnnb1*) in HFD treated group versus LFD. (D) IPA enrichment analysis represented as bubble plot and horizontal bar chart for different cell functions, where activation score (z-score) above two was considered significant (p-value=0.05) and –log 10(p-value) above 1.3 was considered significant (p-value=0.05). N=3. (E) Morphological analysis for cellular perimeter and circularity were measured in each group; one representative image is shown, out of 30 images collected for each experimental condition. N=3. For analysis, 100 cells randomly selected from each replicate for each group were measured using ImageJ. Data were analyzed by unpaired, two-tailed t-test, with statistical significance presented as: ****$p < 0.0001$. All data are shown as mean ± SD. (F) Migration of E0771 cells was measured in a 6-hour transwell assay. Cells that reached the distal side of the 8-µm pore membrane were visualized by crystal violet and microscopy. Quantitative data are from five independent experiments (N=6). (G) Cell counts were performed at 7 and 10 days by hemocytometer and microscopy (N=6). Data were analyzed by unpaired, two-tailed t-test, with statistical significance presented as: ns, not significant. All data are shown as mean ± SD.

Plasma-Derived Exosomes Induce EMT and Enhance Cell Migration and Survival

Further investigation into exosomes derived from plasma revealed significant differential expression of EMT genes (Supplementary Fig. S3A, S3B). Specifically, pro-EMT genes were upregulated while anti-EMT genes were downregulated in cells treated with exosomes from the HFD group (Supplementary Fig. S3C). Notably, the pro-EMT gene *Snai2* showed marked upregulation, and the epithelial marker *Krt14* was significantly downregulated (Fig. 3A-C). These changes suggest a shift towards a mesenchymal phenotype. Enrichment analysis of the differentially expressed genes indicated a negative enrichment for anoikis and cell death pathways, suggesting enhanced cell survival. Conversely, pathways related to cell movement, cytoskeleton organization, and cell viability were the most significantly enriched (Fig. 3D). This enrichment supports the observation that HFD plasma-derived exosomes promote cellular changes conducive to migration and survival, and these pathways are related to activation of RAC1 and STAT3 networks (Supplementary Fig. S3D). Morphological analysis demonstrated that HFD-treated cells exhibited a more mesenchymal-like morphology compared to controls, characterized by elongated cell shapes and increased cytoskeletal reorganization, indicative of a pro-migratory phenotype (Fig. 3E). This morphological shift was further corroborated by migration assays, which confirmed increased cell motility in HFD-treated cells (Fig. 3F). Additionally, cell viability assays revealed higher cell counts in HFD-treated cells after 7 and 10 days of a single exosome treatment (Fig. 3G). This increased viability suggests that exosomes from HFD mice not only promote migration but also enhance cell survival or proliferation. Given these results showing functional differences compared to the adipocyte-derived exosomes, we decided to proceed with plasma-derived exosomes for the rest of the experiments, since they elicit stronger signals in our model.

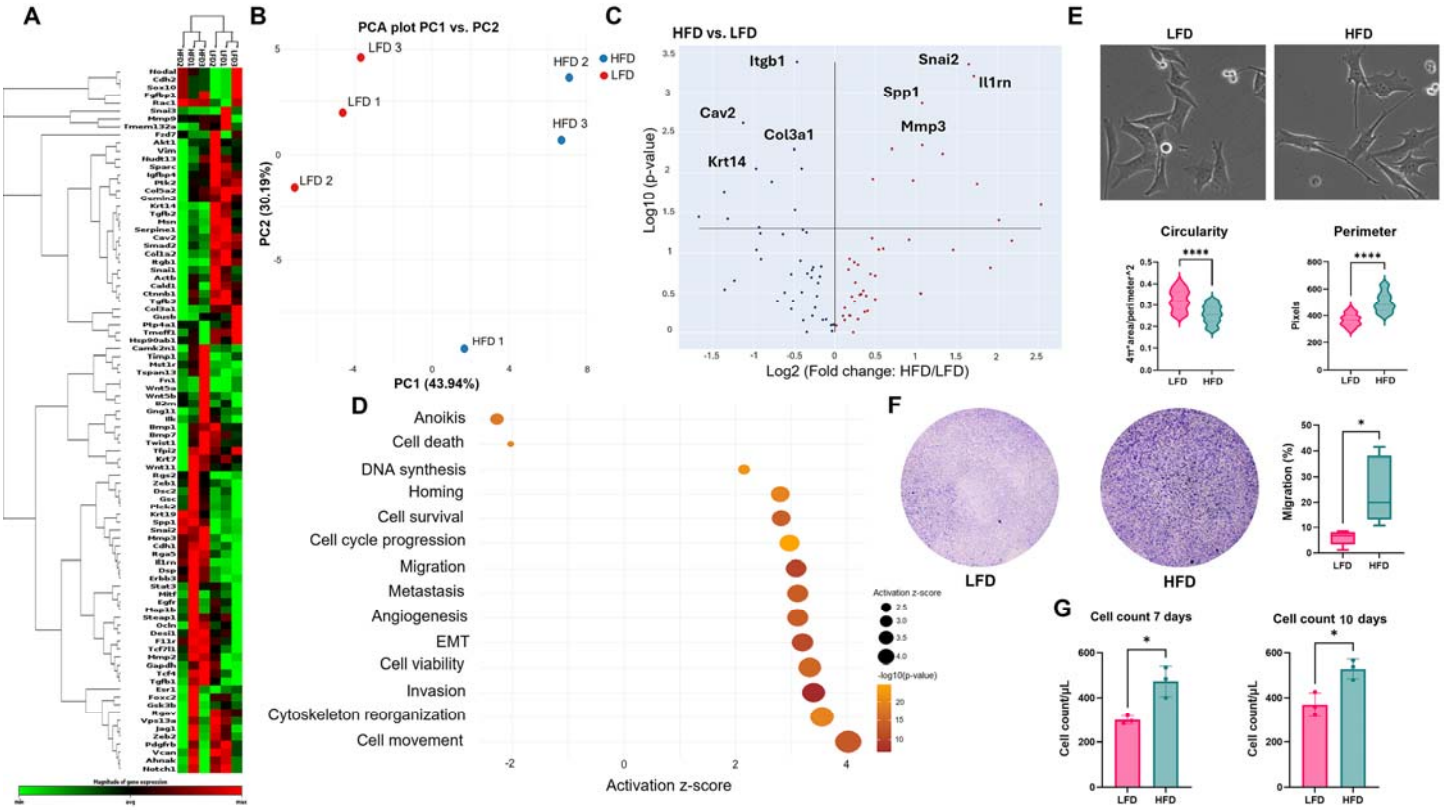

Figure 3. Plasma-derived exosomes from HFD-fed mice induce transcription of EMT genes in E0771 cells

E0771 cells were cultured for 3 days with plasma-derived exosomes of either HFD or LFD fed mice. Expression of selected EMT genes was analyzed by commercial PCR array and IPA. (A) Heatmap of EMT related genes showing differential expression. (B) PCA showing clustering of triplicates of the same group for EMT gene expression. (C) Volcano plot showing significantly upregulated genes (*e.g.*, *Snai2*, *Mmp3*) and downregulated genes (*e.g.*, *Itgb1*, *Krt14*) in HFD treated group versus LFD. (D) IPA enrichment analysis represented as bubble plot and horizontal bar chart for different cell functions, where activation score (z-score) above two was considered significant (p-value=0.05) and –log 10(p-value) above 1.3 was considered significant (p-value=0.05). N=3. (E) Morphological analysis for cellular perimeter and circularity were measured in each group; one representative image is shown, out of 30 images collected for each experimental condition. N=3. For analysis, 100 cells from each replicate for each group were randomly measured using ImageJ. Data were analyzed by unpaired, two-tailed t-test, with statistical significance presented as: ****$p < 0.0001$. All data are shown as mean ± SD. (F) Migration of E0771 cells was measured in a 6-hour transwell assay. Cells that reached the distal side of the 8-µm pore membrane were visualized by crystal violet and microscopy. For quantitation, data are from six independent experiments (N=6). (G) Cell counts were performed at 7 and 10 days by hemocytometer and microscopy (N=3). Data were analyzed by unpaired t-test, two-tailed t-test, with statistical significance presented as: *$p < 0.05$. ns, not significant. All data are shown as mean ± SD.

Proteomic and Phosphoproteomic Profiling of E0771 Cells Treated *in vitro* with Plasma-Derived Exosomes

After observing a stronger effect on cell migration from plasma-derived exosomes, compared to adipocyte-derived exosomes, we proceeded to analyze the proteomic profile of the exosomes to elucidate potential mechanisms underlying the increased cell migration. Proteomic and phosphoproteomic analyses were conducted on samples from HFD and LFD groups to identify differentially expressed proteins and phosphorylation events (Fig. 4A, 4B). The analysis revealed distinct expression profiles between the HFD and LFD groups, with notable differences in proteins involved in cell migration and signaling pathways. Enrichment analysis was performed to identify biological pathways significantly impacted by the differentially expressed proteins. This analysis highlighted significant enrichment in cell migration pathways, particularly those dependent on the Rho-GTPases signaling cascade (Fig. 4C, 4D). Among these, Rac1 was identified as one of the most enriched activation pathways. Rac1 is a well-known regulator of cell motility, cytoskeletal dynamics, and cellular migration, suggesting that its activation may be a key driver of the observed migratory behavior in cells treated with plasma-derived exosomes from the HFD group. Further investigation into the phosphoproteomic data revealed increased phosphorylation of Rac1 and other components of the Rho-GTPases pathway, indicating an upregulation of this signaling cascade in the HFD group. These findings suggest that plasma-derived exosomes from obese mice may promote cell migration through the activation of Rac1 and related pathways, potentially contributing to the aggressive phenotype observed in cancer cells.

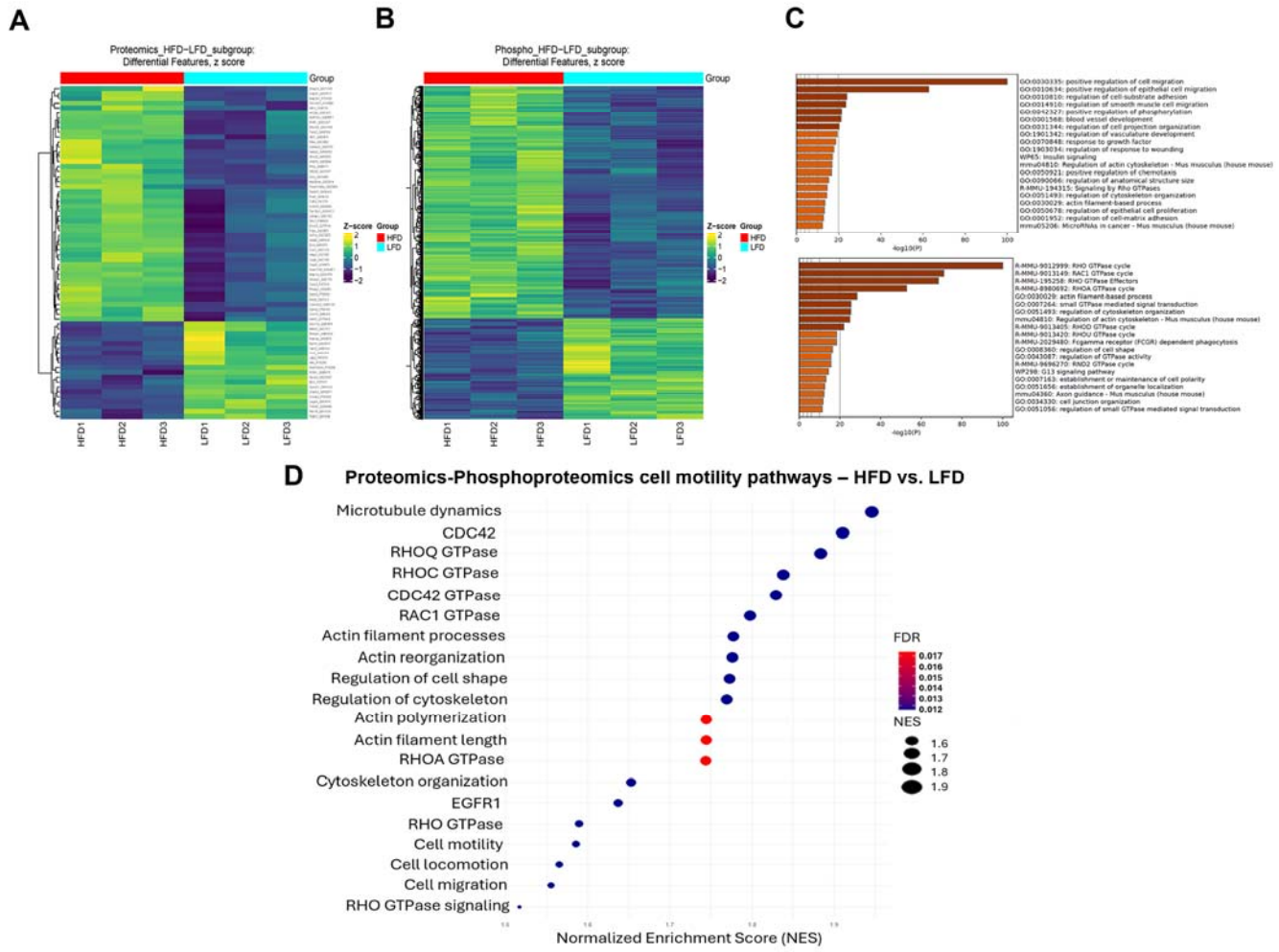

Figure 4. Proteomics and Phosphoproteomics analysis of E0771 cells treated with plasma-derived exosomes.

(A) Proteomics and (B) phosphoproteomics heatmaps showing differential expression features between HFD and LFD groups. (C and D) Enrichment analysis identified biological pathways significantly impacted by the differentially expressed proteins. Bubble plot and horizontal bar chart with NES and –log 10(p-value) above 1.3 considered significant (p-value=0.05). N=3.

Enhanced Metastatic Potential of E0771-GFP Cells Treated with HFD Plasma-Derived Exosomes

To investigate the aggressive mesenchymal phenotype in an animal model, E0771-GFP cells treated with LFD or HFD plasma derived-exosomes for three days were injected into the left second mammary fat pad of six-week-old female C57BL/6J mice. After 28 days, the mice were sacrificed, and the brain and lung tissues

were analyzed (Fig. 5A). Both the lung and brain tissues were homogenized, seeded in cell culture plates, and allowed to grow for 7 days (Fig. 5B). Subsequently, we assessed the number of E0771-GFP colonies (colony count), their size (colony coverage), and their cell density (cell count). Our analyses revealed that both the brain and lung tissues showed a higher number and larger size of colonies in the HFD group compared to the LFD group. Specifically, the brain tissue exhibited a higher cell density in the HFD group, while the lung tissue showed no significant differences in cell density between the groups (Fig. 5C). Notably, in the LFD group, only two out of five mice had brain metastases, whereas all mice in the HFD group showed the presence of E0771 cells in the brain (Supplementary Table S1). However, mice pretreated with HFD exosomes exhibited a significantly higher burden of brain and lung metastases compared to the LFD group (Fig. 5E). These findings suggest that exosomes derived from HFD conditions enhance the metastatic potential of E0771-GFP cells, particularly promoting brain and lung metastasis.

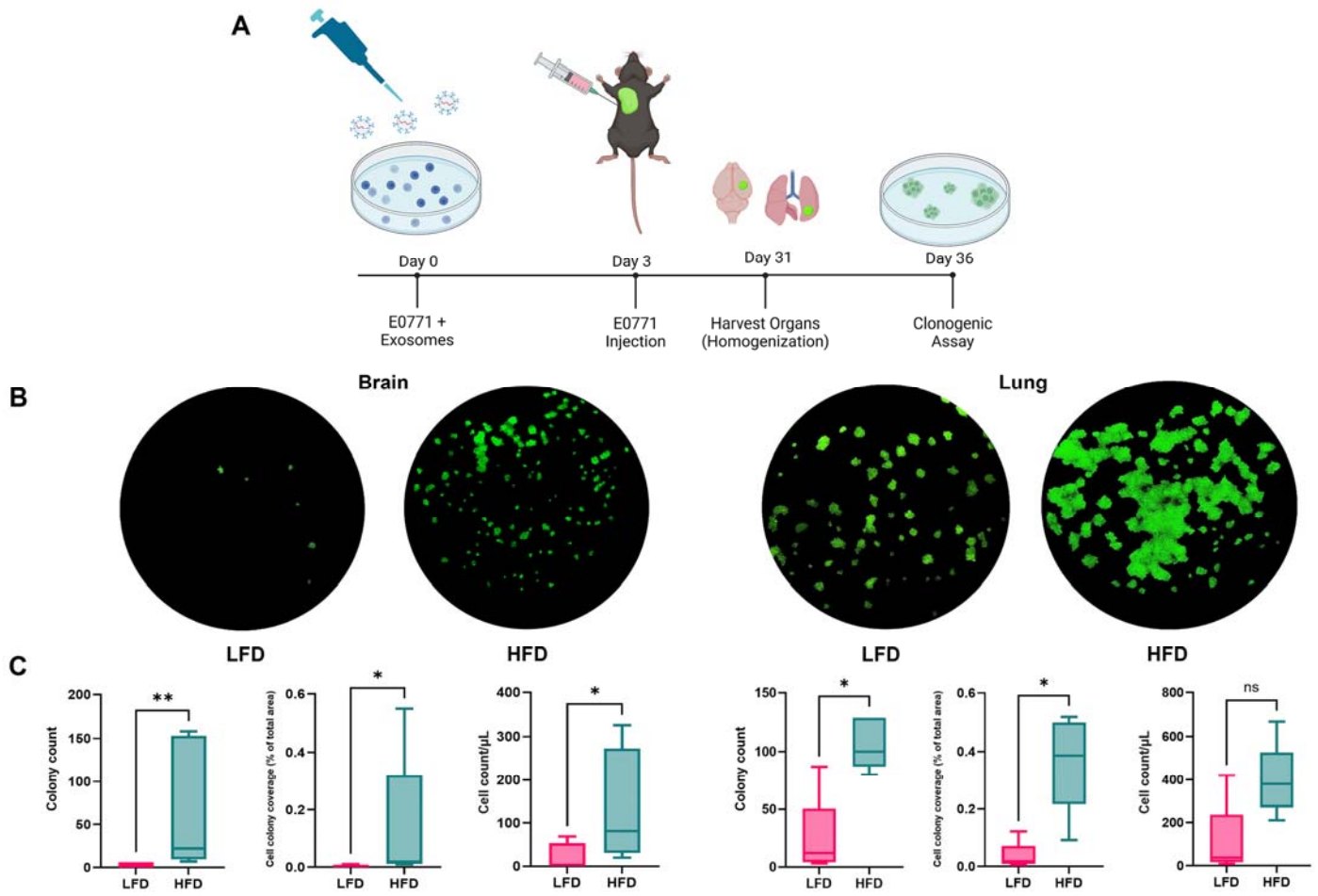

Figure 5. Plasma-derived exosomes from HFD-fed mice promote metastasis burden in brain and lung of C57BL/6J female mice.

E0771 cells were cultured for 3 days with plasma-derived exosomes of either HFD or LFD fed mice, then 100,000 of these cells were injected in the 2nd mammary fat pad of 6-week-old C57BL/6J female mice. Metastases burden was measure by clonogenic assay. (A) Schematic representation of the hybrid *in vitro* and *in vivo* experiment. Image generated with BioRender® software (BioRender.com). (B) Fluorescent microscopy of a chosen representative $10cm^2$ tissue culture plate of a clonogenic assay for both HFD and LFD group and for brain and lung homogenized and tissues (N=5). (C) Statistical comparison for three different parameters accounting for metastasis burden. E0771-GFP cells treated with HFD plasma-derived exosomes show a significant increased metastasis burden compared to the control group (LFD). Data were analyzed by Mann-Whitney test with statistical significance presented as: ns, not significant, *$p < 0.05$; **$p < 0.01$. All data are shown as mean ± SD. N=5.

Transcriptome Analysis of *in vitro* E0771 Cells and Brain Metastatic Cells

Given the significant differences in the brain metastasis burden between HFD and LFD exosome-treated cells. We decided to run Bulk RNA-sequencing on *in vitro* cells 3 days after treatment and before injection in the 2nd mammary fat pad, plus the cells that were obtained from brain metastasis after the 28-day period after injection in the mice. We found a great variety of differentially expressed genes in both brain mets (Fig. 6A) and cells *in vitro* (Fig. 6B) when comparing HFD to LFD treated E0771 cells. Due to the lower incidence of brain metastasis in the LFD treated group, we included a negative control group where E0771-GFP cells were not treated with exosomes to reach an N=5. As expected, LFD (represented as LB group) treated cells and non-exosome treated cells (represented as CB group) clustered together for brain metastatic cells while HFD treated group (represented as HB group) clustered together by itself. Since we observed the LFD treated group was like the negative control, we decided to run enrichment analysis to have a higher power analysis and cluster LFD plus negative control as a one control group versus the HB group. Hallmark gene set enrichment analysis was performed using RNA-seq data from cells treated *in vitro* and from the ones injected into the mammary fat pad of mice that later metastasized to the brain (Fig. 6C). The hypergeometric test revealed significant enrichment of several hallmark gene signatures in both the brain metastasis and *in vitro* conditions, particularly after HFD plasma-derived exosome treatment, as compared to the control groups. *In vitro*, the early estrogen response was significantly downregulated, while in brain metastases, the late estrogen response showed marked downregulation. Additionally, both the glycolysis and hypoxia pathways were notably upregulated in the brain metastasis group following HFD treatment. Immune-related pathways also exhibited significant changes, with both the inflammatory response and interferon alpha/gamma signaling showing strong enrichment in the brain metastasis samples. Finally, mTORC1 signaling was upregulated in brain metastases under HFD conditions, while TNF-alpha signaling via NF-kB was enriched in the *in vitro* cells. To further explore the clinical relevance of these findings, we performed survival analysis using data from both the TCGA (Fig. 6D) and METABRIC

(Supplementary Fig. S4) breast cancer cohorts. Expression levels of genes identified in our study were categorized into high and low expression groups, adjusted for clinical variables such as age and proliferation rates. Kaplan-Meier survival curves from the TCGA cohort demonstrated a significant difference in overall survival between patients with high and low expression of these genes (p = 0.006), with high expression associated with worse survival outcomes. However, analysis of the METABRIC cohort revealed no significant difference between the high and low expression groups (p = 0.8). These results highlight the potential clinical impact of metabolic and immune pathways in brain metastasis, particularly in the context of HFD plasma-

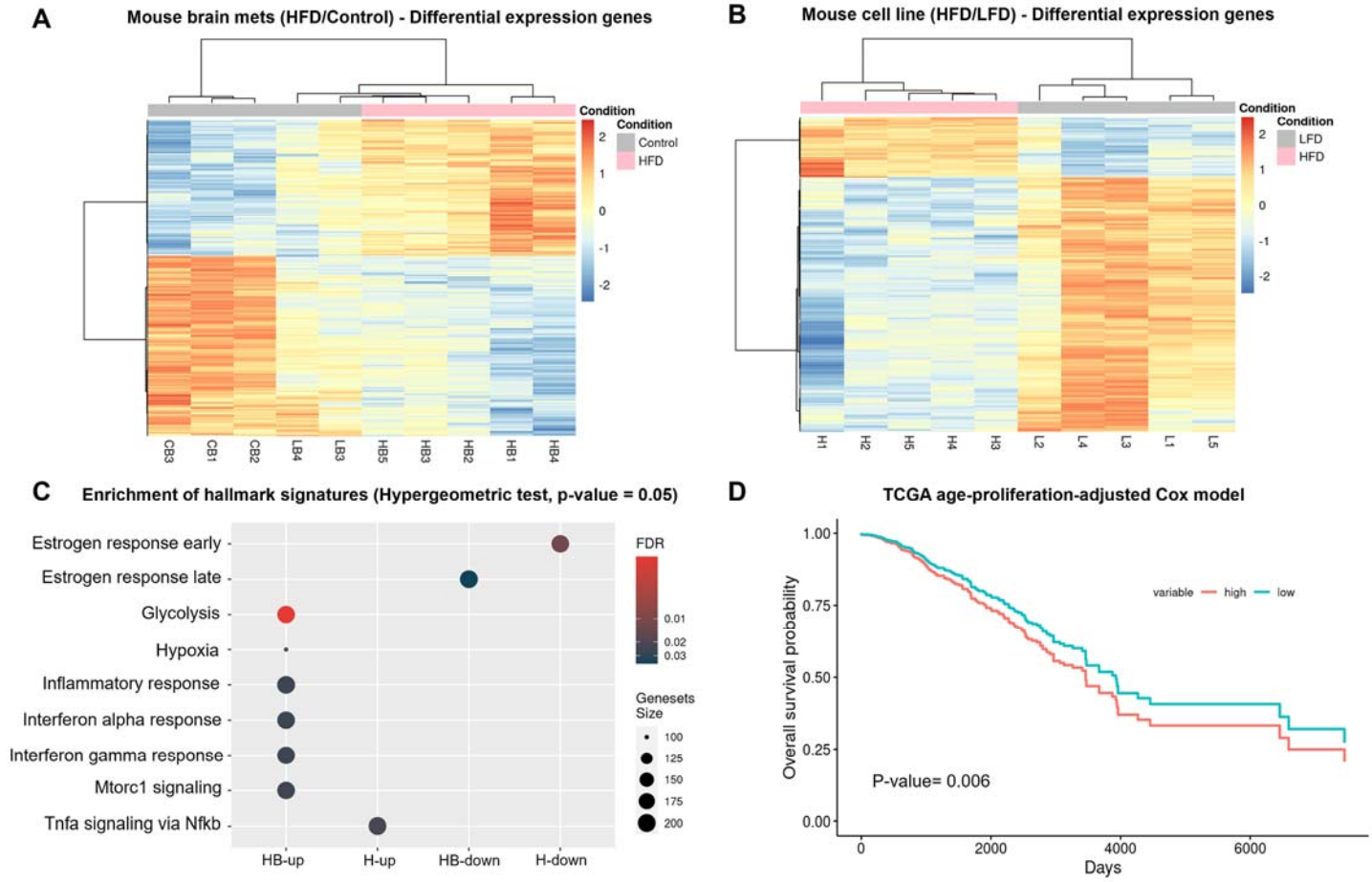

derived exosome treatment.

Figure 6. Transcriptome analysis of *in vitro* and brain metastatic E0771 cells.

(A) Heatmap showing differential gene expression in brain metastatic cells between HFD and control groups. (B) Heatmap of differential expression features in E0771 cells cultured *in vitro* after HFD and control treatments. (C) Enrichment of hallmark gene signatures showing pathways significantly impacted by differential

mRNA expression following treatment. (D) TCGA BRCA-specific survival analysis. Age and Proliferation Adjusted Survival curve of mouse brain metastases (HFD/LFD) showing overall survival probability, with high and low gene expression groups. The difference between groups is statistically significant (P-value = 0.006).

Role of Rac1 in the Mesenchymal and Migratory Phenotype Induced by HFD Exosomes

Given the *in vitro* and *in vivo* effects of HFD exosomes on E0771 cells and the proteomic analysis suggesting a potential mechanism, we investigated the role of Rac1 in the observed mesenchymal phenotype. Cells treated with either HFD or LFD plasma-derived exosomes for 3 days and subsequently with the Rac1 inhibitor, EHT 1864, were tested for the migratory capabilities in a wound-healing assay. Cells were subjected to a dose-response curve for 24 hours. Where EHT 1864 was used in a ranging concentration between 5-50 µM (Supplementary Figs. S5A-C). E0771 cells treated with HFD plasma-derived exosomes and EHT1864 showed an increase migration and wound closure compared to the LFD group (Fig. 7A). A dose-response curve was plotted to determine the IC50 values for both groups, where the IC50 for the LFD group is 26.34 µM and HFD group above 50 µM, observing an increase as well in the area under the curve for the wound closure of the HFD group (Fig. 7B). These differences became more evident the higher the concentration of the Rac1 inhibitor was, as shown in the representative images for each group (Fig. 7C).

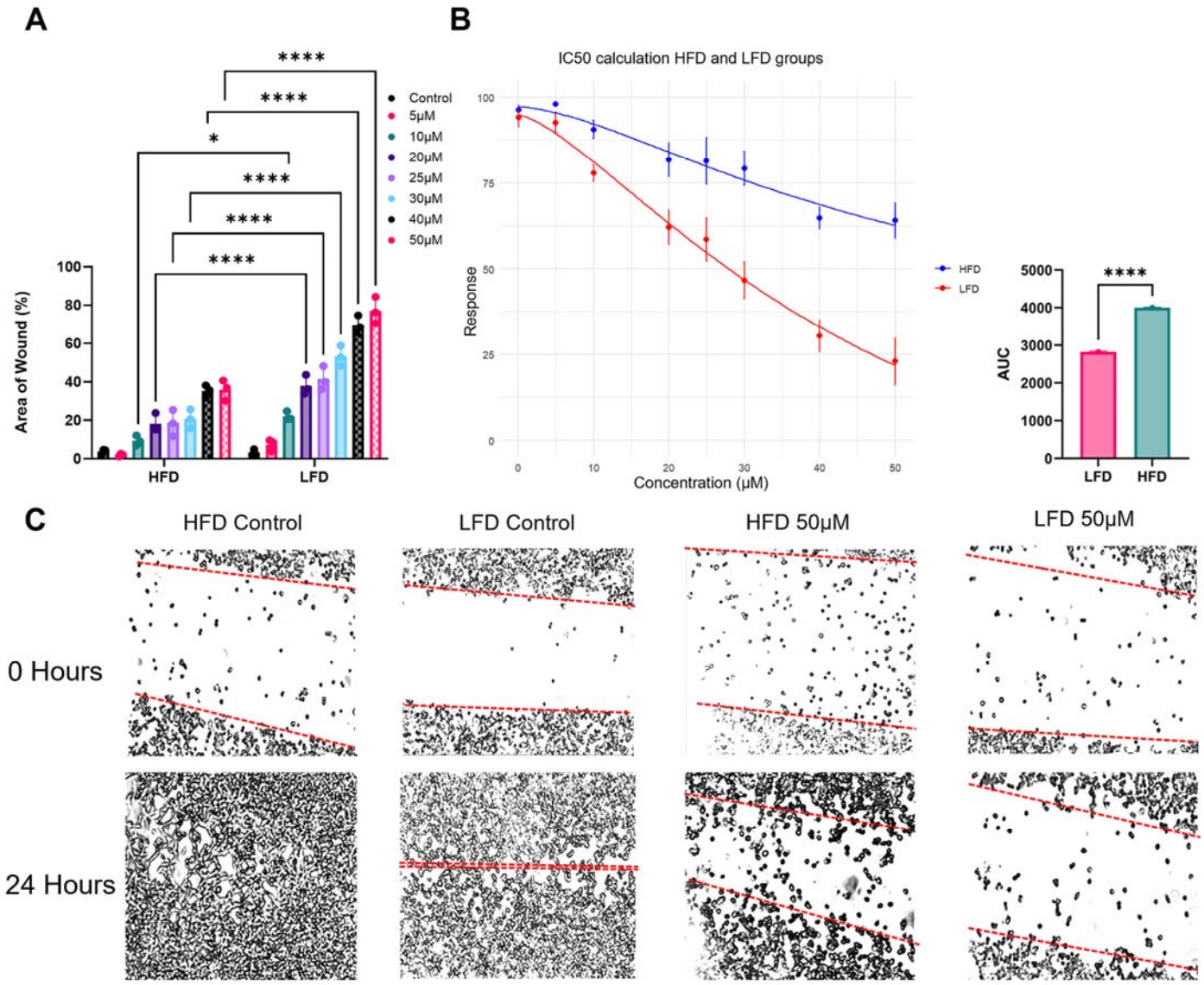

Figure 7. Rac1 role in E0771 cells treated with plasma-derived Exosomes

E0771 cells were cultured for 3 days with plasma-derived exosomes of either HFD or LFD fed mice, after these 3 days, cells were treated with an increasing concentration of the Rac1 inhibitor, EHT1864. Concentrations ranged 5-50 µM, leaving one group as a control without Rac1 inhibitor. (A) Area of the wound represented as a percentage of the total area in time=0. The area of the wound left after 24 hours of the scratch is lower for the cells that were treated with plasma-derived HFD exosomes, indicating and increase in the closure of the wound. Data were analyzed by 2-way Anova with a Šidák's post-hoc analysis for multiple comparison testing with statistical significance presented as: *$p < 0.05$; ****$p < 0.0001$. All data are shown as mean ± SD. (B) Dose-response curve for different EHT1864 concentrations (0, 5, 10, 20, 25, 30, 40 and 50 µM). The area under the curve between both groups shows a statistical difference between the level of response to EHT1864 inhibitor. Data were analyzed by unpaired, two-tailed t-test, with statistical significance presented as: ****$p < 0.0001$. All data are shown as mean ± SD. (C) Representative images of the wound-closure assay at 0 hours and 24 hours

after the scratch. These images show the differential closure between HFD and LFD at high concentrations of EHT 1864. N=3.

DISCUSSION

Population studies over the past twenty years have strongly implicated obesity and diabetes as risk factors in the incidence and progression of obesity-driven cancers, including breast cancer (23,24). However, the key causal elements that connect obesity-driven, systemic insulin resistance to increased metastatic burden and tumor progression remain poorly understood. As other groups have described (25, 26), the growth of E0771 tumors is enhanced in obese mice compared to lean mice, and we have separately shown that plasma or adipocyte derived exosomes that reflect diabetic or insulin resistant features of obesity strongly promote tumor aggressiveness in multiple cancer types (14, 15, 16) which lead us to hypothesize that exosomes either present in plasma or derived from adipocyte exosomes promote tumor growth and aggressiveness. In this study, we utilized an HFD-fed C57BL/6J mouse model to investigate the impact of obesity-driven insulin resistance on exosome production and function, focusing particularly on the role of exosomes in promoting a mesenchymal phenotype in E0771 cells as a model for triple negative breast cancer in women with obesity-driven metabolic disease.

Our results demonstrate that HFD-induced obesity and insulin resistance significantly alter exosomal content, leading to profound molecular and phenotypic changes in breast cancer cells, compared to lean and insulin sensitive controls. We first demonstrated that the HFD-induced obesity model was successfully established, evidenced by standard methods of validation like oGTT and ipITT to confirm systemic insulin resistance, by showing abnormalities in glucose clearance and insulin responsiveness respectively (27,28), significant weight gain and increased body weight (29).

Exosomes isolated from HFD-treated mice promoted an EMT signature of breast cancer cells distinct and significantly worse than LFD controls. EMT array analysis revealed upregulation of key EMT markers, such as Snai1 and Ctnnb1, and morphological changes indicative of mesenchymal phenotype and enrichment of

pathways related to cytoskeleton organization, migration, and cell survival. This pattern has been already reported by different groups, where cell morphology and migration are linked to upregulation of EMT genes, including the genes mentioned above (30,31). Despite these molecular changes, migration assays showed no functional difference in migratory capacity under the tested conditions. This discrepancy suggests that whereas HFD-derived exosomes induce molecular markers of EMT, additional factors or conditions are required to translate these transcriptional changes into enhanced migratory behavior.

Further analysis of plasma-derived exosomes from HFD-treated mice showed significant upregulation of pro-EMT genes and downregulation of epithelial markers, indicating a shift towards a mesenchymal phenotype. These exosomes enhanced cell motility, viability and migratory capability, suggesting a more pronounced role in promoting cancer progression compared to adipocyte-derived exosomes. These findings underscore the importance of the source of exosomes and suggest that plasma-derived exosomes have a more significant role in promoting aggressive cellular behaviors.

Proteomic and phosphoproteomics analyses further highlighted the involvement of Rac1 and the Rho-GTPase signaling cascade, which is a known regulator of cell motility and cytoskeletal dynamics (32, 33, 34). The upregulation of Rac1 and Rho-GTPase pathways aligns with increased cell motility and mesenchymal transition, suggesting that these signaling pathways are potential mediators of the pro-EMT effects induced by HFD exosomes.

In vivo experiments using E0771-GFP cells treated with HFD or LFD plasma-derived exosomes demonstrated a higher metastatic burden in the brain and lungs of mice under the HFD condition. These results are consistent with previous clinical studies, where patients with TNBC and comorbid obesity face increased risk of developing secondary tumors in the brain (35), suggesting that plasma exosomes may enhance the brain metastatic potential of breast cancer patients with obesity. The greater number and size of colonies in the brain

and lungs in our model, particularly the universal presence of brain metastases in the HFD group, highlight the aggressive nature of the cancer cells influenced by these exosomes.

RNA-seq results highlight downregulation of early estrogen response *in vitro* and late estrogen response in brain metastases, consistent with the ER-negative nature of E0771 cells (36). This pattern suggests the cells have become estrogen-independent, characteristic of TNBC. Additionally, significant enrichment of glycolysis and hypoxia pathways in the brain metastases points to metabolic reprogramming (37, 38), where tumor cells adopt aerobic glycolysis to survive in the nutrient-deprived and hypoxic brain environment, a key adaptation that might favor E0771 cells treated with HFD plasma-derived exosomes to colonize and form a higher metastatic burden in brain compared to the control group. Survival analysis using the TCGA breast cancer cohort further underscores the potential clinical relevance of these metabolic and immune alterations, with high expression of the genes identified in the mouse model being significantly associated with worse overall survival outcomes among patients. This finding suggests that the pathways modulated by HFD-derived exosome treatment in our mouse models may have translational relevance to certain subtypes of human breast cancer, particularly those captured in the TCGA cohort. In contrast, the METABRIC analysis did not reveal a significant survival difference, suggesting that these gene expression changes may be prognostic for human breast cancer depending on specific breast cancer subtypes or patient cohorts. Overall, our RNA-seq analysis identified metabolic and immune-related changes, such as enrichment of inflammatory response and interferon alpha/gamma signaling, between HFD and LFD exosome-treated cells. These findings should be validated in more complex *in vivo* systems. Given this focus on immune modulation, the pathway directionality was not strong nor specific.

However, proteomics analysis revealed robust activation of Rac1 and Rho GTPase signaling, which are crucial for cytoskeletal reorganization, migration and metastasis. In addition, Rho GTPases are thought to play a role in establishing an immunosuppressive tumor microenvironment (39), which links both observations. In the setting of obesity and insulin resistance, Rho GTPases contribute to glucose homeostasis by performing critical

metabolic functions within skeletal muscle and adipose tissue (40,41). These findings led us to prioritize these pathways for further investigation, given their established role in driving tumor invasion and brain metastasis. Further investigation into the role of Rac1 revealed its critical involvement in promoting the mesenchymal and migratory phenotype observed in HFD-treated cells. The use of the Rac1 inhibitor EHT-1864 (42, 43) demonstrated dose-dependent inhibition of migration and wound closure, with HFD-treated cells exhibiting higher resistance to Rac1 inhibition.

The role of Rho GTPases, particularly Rac1, in cancer progression is increasingly recognized as a critical factor in driving breast cancer metastasis (44). Moreover, ongoing clinical trials, currently in Phase 1, investigate the use of oral MBQ-167 (a compound targeting Rho GTPases) as a single agent for participants with advanced breast cancer (45). Therefore, Rho GTPases and Rac1 could serve as critical mediators linking the metabolic dysfunction caused by obesity and systemic insulin resistance with the increased metastatic potential of TNBC. This understanding positions Rac1 as a promising therapeutic target, particularly in patients with obesity-related metabolic comorbidities, providing a rationale for further exploration of Rac1 inhibition in mitigating metastatic burden. Considering the large burden of obesity and metabolic disease among adult Americans, with >120 million people currently diagnosed as diabetic or pre-diabetic (46), the public health significance of these insights for breast cancer patients is apparent.

Our study provides compelling evidence that exosomes derived from HFD-fed mice significantly promote breast cancer progression and metastasis. These findings underscore the critical role of metabolic conditions in modulating exosomal content and their subsequent impact on cancer cell behavior. The differential effects observed between exosomes derived from visceral adipose tissue and plasma suggest that circulating exosomes may have a more pronounced impact on promoting a mesenchymal and metastatic phenotype in TNBC cells. Future research should explore therapeutic strategies targeting specific signaling pathways, such as Rac1, to mitigate the pro-metastatic effects of obesity-driven insulin resistance.

Acknowledgements

We thank Boston University-Boston Medical Center Cancer Center faculty R. Flynn, N. Ganem and Valentina Perissi, for helpful comments and suggestions. We thank Anna Belkina, Shari Brezinsky and Brian Tilton, the BUMC Flow Cytometry Core Facility, Matthew Bo Au of the BUMC Analytical Core Facility. Thank you to Timothy Padera and Hengbo Zhou for donating the cell line E0771-GFP. We would also like to thank Nabil Rabhi for his recommendations in animal handling, procedures like mice blood extraction, glucose and insulin tests. This work was supported by the Cancer Moonshot and Cancer Systems Biology Consortium of the National Cancer Institute (G.V.D.: U01CA182898, U01CA243004, and R01CA222170)

References

1. Giaquinto AN, Sung H, Newman LA, et al. Breast cancer statistics 2024. *CA Cancer J Clin*. 2024; 1-19.
2. Foulkes, W. D., Smith, I. E., & Reis-Filho, J. S. (2010). Triple-negative breast cancer. New England Journal of Medicine, 363(20), 1938-1948.
3. Bianchini, G., Balko, J. M., Mayer, I. A., Sanders, M. E., & Gianni, L. (2016). Triple-negative breast cancer: challenges and opportunities of a heterogeneous disease. Nature Reviews Clinical Oncology, 13(11), 674-690.
4. Henry NL, Shah PD, Haider I, Freer PE, Jagsi R, Sabel MS. Chapter 88: Cancer of the Breast. In: Niederhuber JE, Armitage JO, Doroshow JH, Kastan MB, Tepper JE, eds. Abeloff's Clinical Oncology. 6th ed. Philadelphia, Pa: Elsevier; 2020. Included in: American Cancer Society. (2020). Breast Cancer Survival Rates.
5. Perrone, M. A., Pierdominici, M., Parrinello, G., Malorni, W., & Salerno, G. (2021). Metabolic diseases and breast cancer: the interplay between tumor microenvironment and cellular metabolism. Cancers, 13(5), 963.
6. Kolb, R., Zhang, W., & DeAngelis, T. (2018). Obesity and cancer: inflammation bridges the two. Current Opinion in Pharmacology, 42, 87-102.
7. Park, J., Euhus, D. M., & Scherer, P. E. (2011). Paracrine and endocrine effects of adipose tissue on cancer development and progression. Endocrine Reviews, 32(4), 550-570.
8. Park, J., Morley, T. S., Kim, M., Clegg, D. J., & Scherer, P. E. (2014). Obesity and cancer—mechanisms underlying tumour progression and recurrence. Nature Reviews Endocrinology, 10(8), 455-465.
9. Brown, K. A., Simpson, E. R., & Rudnicka, C. (2010). Obesity and breast cancer: mechanisms underlying risk and response to treatment. Frontiers in Endocrinology, 1, 26.

10. Sun, X., Casbas-Hernandez, P., Bigelow, C., Makowski, L., Joseph Jerry, D., & Troester, M. A. (2012). Normal breast tissue of obese women is characterized by an inflammatory signature. Breast Cancer Research and Treatment, 131(3), 1021-1037.
11. Kalluri, R., & LeBleu, V. S. (2020). The biology, function, and biomedical applications of exosomes. Science, 367(6478), eaau6977.
12. Guay, C., Kruit, J. K., Rome, S., Menoud, V., Mulder, N. L., Jurdzinski, A., ... & Regazzi, R. (2019). Lymphocyte-derived exosomes promote β-cell death in type 1 diabetes. Diabetes, 68(9), 1782-1793.
13. Costa-Silva, B., Aiello, N. M., Ocean, A. J., Singh, S., Zhang, H., Thakur, B. K., ... & Lyden, D. (2015). Pancreatic cancer exosomes initiate pre-metastatic niche formation in the liver. Nature Cell Biology, 17(6), 816-826.
14. Jafari N, Kolla M, Meshulam T, Shafran JS, Qiu Y, Casey AN, Pompa IR, Ennis CS, Mazzeo CS, Rabhi N, Farmer SR, Denis GV. Adipocyte-derived exosomes may promote breast cancer progression in type 2 diabetes. Sci Signal. 2021 Nov 23;14(710):eabj2807.
15. Jafari N, Chen A, Kolla M, Pompa IR, Qiu Y, Yu R, Llevenes P, Ennis CS, Mori J, Mahdaviani K, Halpin M, Gignac GA, Heaphy CM, Monti S, Denis GV. Novel plasma exosome biomarkers for prostate cancer progression in co-morbid metabolic disease. Adv Cancer Biol Metastasis. 2022 Dec;6:100073.
16. Jafari N, Llevenes P, Denis GV. Exosomes as novel biomarkers in metabolic disease and obesity-related cancers. Nat Rev Endocrinol. 2022 Jun;18(6):327-328.
17. Patel H, Ewels P, Manning J, Garcia MU, Peltzer A, Hammarén R, Botvinnik O, Talbot A, Sturm G, nf-core bot, Zepper M, Moreno D, Vemuri P, Binzer-Panchal M, silviamorins, Pantano L, Syme R, Kelly G, Hanssen F, Fellows Yates JA, Espinosa-Carrasco J, Fenouil R, Zappia L, Cheshire C, Miller E, Hoeppner M, Zhou P, Guinchard S, Gabernet G, Mertes C. nf-core/rnaseq: nf-core/rnaseq v3.15.1 - Augmented Aluminium Axolotl (Version 3.15.1) [Software]. Zenodo. 2024.

18. Love MI, Huber W, Anders S. Moderated estimation of fold change and dispersion for RNA-seq data with DESeq2. Genome Biol. 2014;15:550.
19. Therneau TM. A package for survival analysis in R. R package version 3.5-7. 2023.
20. The Cancer Genome Atlas Network. Comprehensive molecular portraits of human breast tumours. Nature. 2012;490:61–70.
21. Curtis C, Shah SP, Chin SF, Turashvili G, Rueda OM, Dunning MJ, Speed D, Lynch AG, Samarajiwa S, Yuan Y, Gräf S, Ha G, Haffari G, Bashashati A, Russell R, McKinney S, METABRIC Group, Langerød A, Green A, Provenzano E, Wishart G, Pinder S, Watson P, Markowetz F, Murphy L, Ellis I, Purushotham A, Børresen-Dale AL, Brenton JD, Tavaré S, Caldas C, Aparicio S. The genomic and transcriptomic architecture of 2,000 breast tumours reveals novel subgroups. Nature. 2012;486:346–352.
22. Venet D, Dumont JE, Detours V. Most random gene expression signatures are significantly associated with breast cancer outcome. PLOS Comput Biol. 2011;7(10)
23. Konstantinos I. Avgerinosa, Nikolaos Spyrou, Christos S. Mantzorosb, Maria Dalamaga. Obesity and cancer risk: Emerging biological mechanisms and perspectives. Metabolism Clinical and Experimental 92 (2019) 121–135.
24. Dae-Seok Kim, Philipp E. Scherer. Obesity, Diabetes, and Increased Cancer Progression. Review. Diabetes Metab J 2021;45:799-812.
25. Esther Hermano, Rachel Goldberg, Ariel M. Rubinstein, Amir Sonnenblick, Bella Maly, Daniela Nahmias, Jin-Ping Li, Marinka A.H. Bakker, Johan van der Vlag, Israel Vlodavsky, Tamar Peretz, Michael Elkin; Heparanase accelerates obesity-associated breast cancer progression. Cancer Res 2019; canres.4058.2019.
26. Maguire, O. A., Ackerman, S. E., Szwed, S. K., Maganti, A. V., Marchildon, F., Huang, X., ... & Cohen, P. (2021). Creatine-mediated crosstalk between adipocytes and cancer cells regulates obesity-driven breast cancer. Cell metabolism, 33(3), 499-512.

27. Csörsz Nagy, Elisa Einwallner. Study of In Vivo Glucose Metabolism in High-fat Diet-fed Mice Using Oral Glucose Tolerance Test (OGTT) and Insulin Tolerance Test (ITT). J Vis Exp. 2018; (131): 56672. Published online 2018 Jan 7.
28. Kleinert, M., Clemmensen, C., Hofmann, S. M., Moore, M. C., Renner, S., Woods, S. C.,Tschöp, M. H. (2018). Animal models of obesity and diabetes mellitus. Nature Reviews Endocrinology, 14(3), 140–162.
29. Nahmias Blank, D.; Hermano, E.; Sonnenblick, A.; Maimon, O.; Rubinstein, A.M.; Drai, E.; Maly, B.; Vlodavsky, I.; Popovtzer, A.; Peretz, T.; et al. Macrophages Upregulate Estrogen Receptor Expression in the Model of Obesity-Associated Breast Carcinoma. Cells 2022, 11, 2844.
30. Moreno-Bueno, G., Peinado, H., Molina, P. et al. The morphological and molecular features of the epithelial-to-mesenchymal transition. Nat Protoc 4, 1591–1613 (2009).
31. Cervantes-Arias, A., Pang, L.Y. and Argyle, D.J. (2013), Epithelial-mesenchymal transition as a fundamental mechanism underlying the cancer phenotype. Vet Comp Oncol, 11: 169-184.
32. Parri, M., Chiarugi, P. Rac and Rho GTPases in cancer cell motility control. Cell Commun Signal 8, 23 (2010).
33. Anne J. Ridley; Rho GTPases and cell migration. J Cell Sci 1 August 2001; 114 (15): 2713–2722.
34. Torsten Wittmann, Clare M. Waterman-Storer; Cell motility: can Rho GTPases and microtubules point the way?. J Cell Sci 1 November 2001; 114 (21): 3795–3803.
35. Gourgue F, Mignion L, Van Hul M, et al. Obesity and triple-negative-breast-cancer: Is apelin a new key target?. J Cell Mol Med. 2020; 24: 10233–10244.
36. Yelek, C.; Mignion, L.; Paquot, A.; Bouzin, C.; Corbet, C.; Muccioli, G.G.; Cani, P.D.; Jordan, B.F. Tumor Metabolism Is Affected by Obesity in Preclinical Models of Triple-Negative Breast Cancer. Cancers 2022, 14, 562.

37. Sriram Venneti, and Craig B. Thompson. Metabolic Reprogramming in Brain Tumors. Review. Annual Review of Pathology: Mechanisms of Disease Volume 12, 2017.

38. Gouirand V, Guillaumond F and Vasseur S (2018) Influence of the Tumor Microenvironment on Cancer Cells Metabolic Reprogramming. Front. Oncol. 8:117.

39. Yang, Q., Zhuo, Z., Qiu, X. et al. Adverse clinical outcomes and immunosuppressive microenvironment of RHO-GTPase activation pattern in hepatocellular carcinoma. J Transl Med 22, 122 (2024).

40. Møller LLV, Klip A, Sylow L. Rho GTPases-Emerging Regulators of Glucose Homeostasis and Metabolic Health. Cells. 2019 May 9;8(5):434.

41. Machin, P.A.; Tsonou, E.; Hornigold, D.C.; Welch, H.C.E. Rho Family GTPases and Rho GEFs in Glucose Homeostasis. Cells 2021, 10, 915.

42. Adam Shutes, Cercina Onesto, Virginie Picard, Bertrand Leblond, Fabien Schweighoffer, Channing J. Der. Specificity and Mechanism of Action of EHT 1864, a Novel Small Molecule Inhibitor of Rac Family Small GTPases. Mechanisms of Signal Transduction. Journal of Biological Chemistry. Volume 282, Issue 49, 7 December 2007, Pages 35666-35678.

43. Vincent Sauzeau, Julien Beignet, Gérard Vergoten, Christian Bailly. Overexpressed or hyperactivated Rac1 as a target to treat hepatocellular carcinoma. Pharmacological Research. Volume 179, May 2022, 106220.

44. Humphries B, Wang Z, Yang C. Rho GTPases: Big Players in Breast Cancer Initiation, Metastasis and Therapeutic Responses. Cells. 2020 Sep 25;9(10):2167.

45. ClinicalTrials.gov. (2024). A Phase 1 open-label, first-in-human trial of oral MBQ-167 as a single agent in participants with advanced breast cancer (Identifier NCT06075810). ClinicalTrials.gov.

46. Wagenknecht LE, Lawrence JM, Isom S, et al. Trends in incidence of youth-onset type 1 and type 2 diabetes in the USA, 2002-18: results from the population-based SEARCH for Diabetes in Youth study. *Lancet Diabetes Endocrinol*. 2023;11(4):242–250.

Plasma Exosomes in Obesity-driven Diabetes Exacerbate Progression of Triple Negative Breast Cancer

Pablo Llevenes, Andrew Chen, Matthew Lawton, Yuhan Qiu, Michael Seen,
Stefano Monti, and Gerald V. Denis

Supplementary Information

Supplementary Data and Figures

In addition to the main findings presented in this manuscript, further data is provided in supplementary materials.

- Supplementary Table S2: Prot_Phos_Summary — This table contains a comprehensive summary of the proteomics analysis, detailing the normalized Log2 intesity protein states observed in both the HFD and LFD experimental conditions.
- Supplementary Table S3: Combined_HFD_LFD_Mouse_GOBP_AllPathways — This table includes results from the Gene Ontology Biological Process pathway enrichment analysis using the Fast Gene Set Enrichment Analysis method. It combines data from HFD and LFD exosome-treated mice, highlighting all enriched pathways.

Supplementary Figures

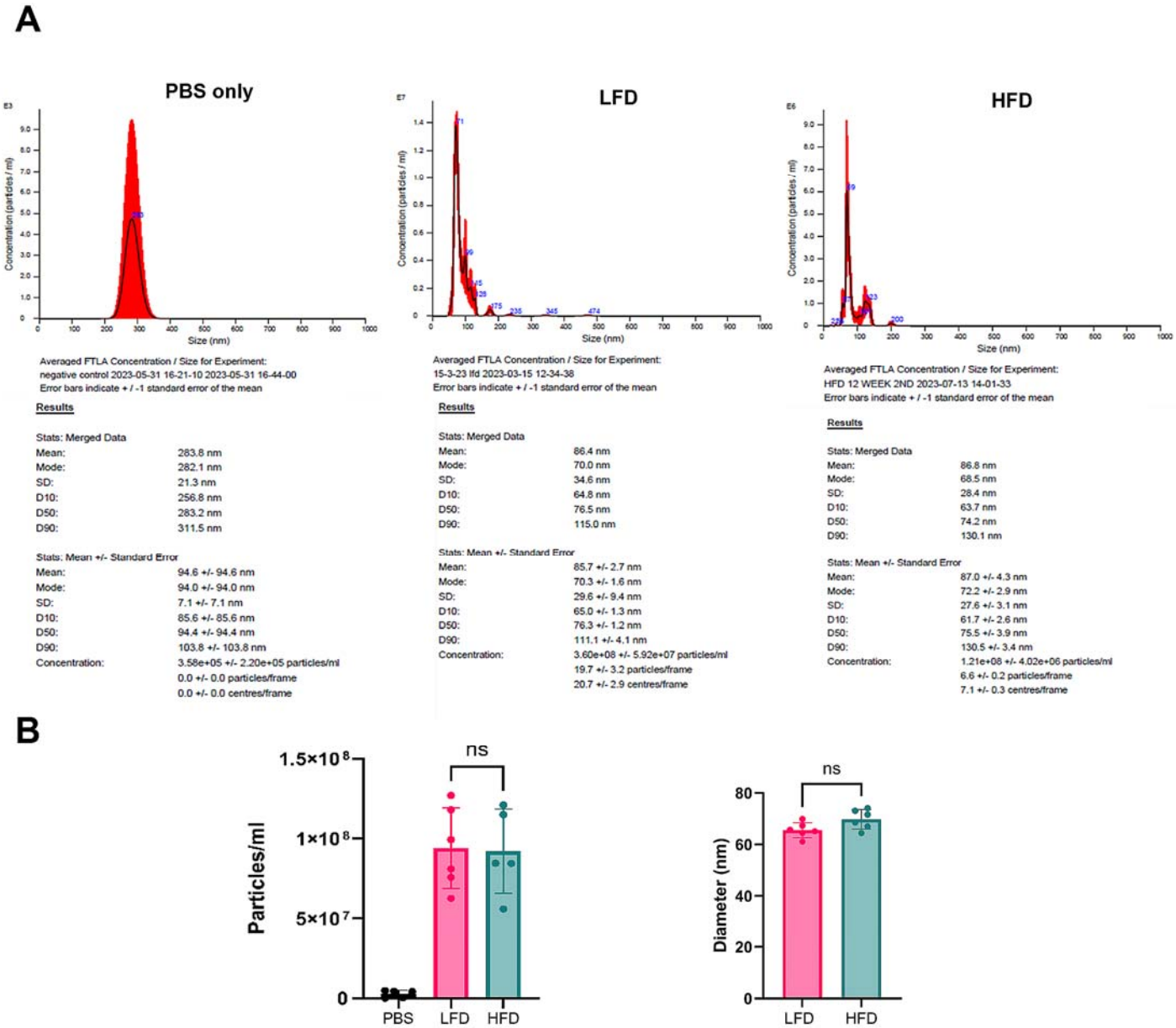

Supplementary Figure S1: Plasma-derived exosome profiling control experiments using NanoSight NS300.

(A) NanoSight NS300 size fractionation of plasma-origin exosomes. Total exosomes were purified from blood plasma of HFD and LFD fed mouse, resuspended in phosphate buffered saline pH 7.4 (PBS) and then analyzed by NanoSight NS300 to determine concentration and particle sizes. (B) Exosomes were analyzed quantitative and qualitatively, to determine their size distribution and abundance. Abundance was measured as particles/mL and mode was considered as the size distribution for each sample. Filtered PBS vehicle was used as a negative control for particle abundance. Data are mean ± SD from N=6 independent experiments. Where ns not significant by unpaired, two-tailed t-test compared to LFD control.

A

Test Group	Control Group	Fold Regulation Threshold	p-Value Threshold
HFD	LFD	1	0.05

Position	Gene Symbol	Fold Regulation	p-Value	Comments
A01	Ahnak	1.21	0.043891	
B01	Ctnnb1	1.49	0.000098	
B06	Esr1	1.42	0.042737	A
B10	Foxc2	1.35	0.041989	
B12	Gng11	1.87	0.013219	
D06	Mstlr	1.70	0.002550	
D12	Pdgfrb	1.85	0.044334	
E10	Snai1	1.38	0.000101	
F10	Tgfb2	1.27	0.017537	
F11	Tgfb3	1.14	0.009651	
H03	Gapdh	1.50	0.004050	

B

Test Group	Control Group	Fold Regulation Threshold	p-Value Threshold
HFD	LFD	1	0.05

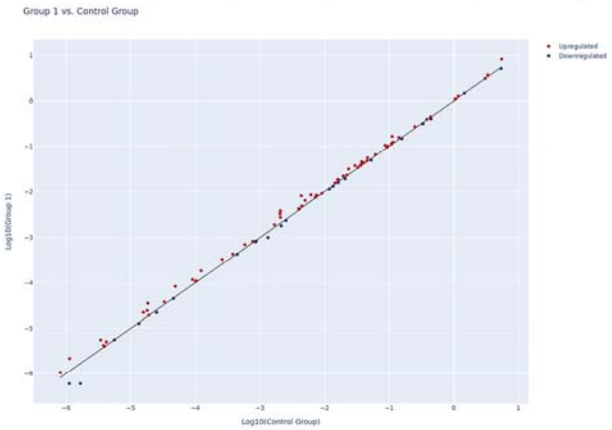

C

Visualization of log2(Fold Change)

Test Group	Control Group
HFD	LFD

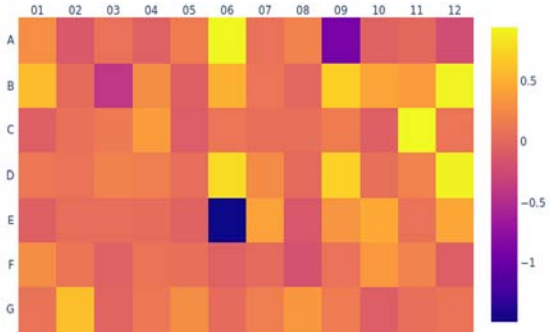

Layout	01	02	03	04	05	06	07	08	09	10	11	12
A	Ahnak / 1.21	Akt1 / -1.1	Bmp1 / 1.05	Bmp2 / -1.04	Cadf1 / 1.11	Camk2n1 / 1.9 / B	Cav2 / 1.05	Cdh1 / 1.14	Cdh2 / -1.88 / B	Col1a2 / -1.04	Col3a1 / -1.1	Col4a2 / -1.17
B	Ctnnb1 / 1.49	Dsc2 / 1.02 / B	Dsp / -1.32	Egfr / 1.2	Erbb3 / -1.06	Esr1 / 1.42 / A	F11r / 1.07	Fgfbp1 / -1.0 / B	Fn1 / 1.61 / B	Foxc2 / 1.35	Fut7 / 1.29 / B	Gng11 / 1.87
C	Gsc / -1.05 / B	Gsk3b / 1.05	Igfbp4 / 1.09	Il1rn / 1.29	Itk / -1.07	Itga5 / 1.07	Itgav / 1.13	Itgb1 / 1.04	Itg1 / 1.11	Krt19 / 1.05	Krt19 / 1.38 / A	Krt7 / 1.07
D	Mif / 1.08	Mmp2 / 1.06	Mmp3 / 1.14	Mmp9 / 1.32	Mrc / 1.03	Mstlr / 1.7	Mapk8 / 1.2	Nodal / 1.03 / A	Notch1 / 1.03	Nudt13 / 1.08	Ocln / 1.15	Pdgfrb / 1.85
E	Pik3 / -1.05	Plau / 1.03	Prk5 / 1.03	Psmb4 / 1.02	Rac1 / -1.04	Rgs3 / -1.8 / B	Sastpmt / 1.11	Cyntin2 / -1.1	Snai1 / 1.25	Snai2 / 1.38	Snai3 / 1.05	Vim / 1.38 / A
F	Sod1 / 1.2 / B	Sparc / 1.07	Spp1 / -1.05	Stat3 / 1.06	Stmp1 / 1.04	Tcf4 / -1.05	Tcf7l1 / 1.0	Tlr2 / -1.14	Tgfb1 / 1.05	Tgfb2 / 1.27	Tgfb3 / 1.14	Timp1 / -1.05
G	Tnfrsf1 / 1.06	Tmem132a / 1.51	Tgfbrl3 / -1.03	Twist1 / 1.08	Vcan / 1.2	Vim / 1.03	Vps13a / 1.12	Wnt1 / 1.27	Wnt5a / 1.1 / B	Wnt5b / -1.06	Zeb1 / 1.04	Zeb2 / 1.06

Supplementary Figure S2: EMT array gene expression and upregulated pathways in HFD adipocyte-derived exosomes.

(A) Fold regulation gene expression of E0771 significantly upregulated genes in HFD v.s. LFD adipocyte derived exosomes. (B) Scatter plot of HFD v.s. LFD adipocyte-derived exosomes. (C) Visualization of log2 (fold change) gene expression as a heatmap comparing HFD v.s. LFD. (Gene expression tables and plots were generated by Qiagen RT2 profiler online software. A p-value <0.05 and fold regulation >1 was considered for gene expression analysis and significant.

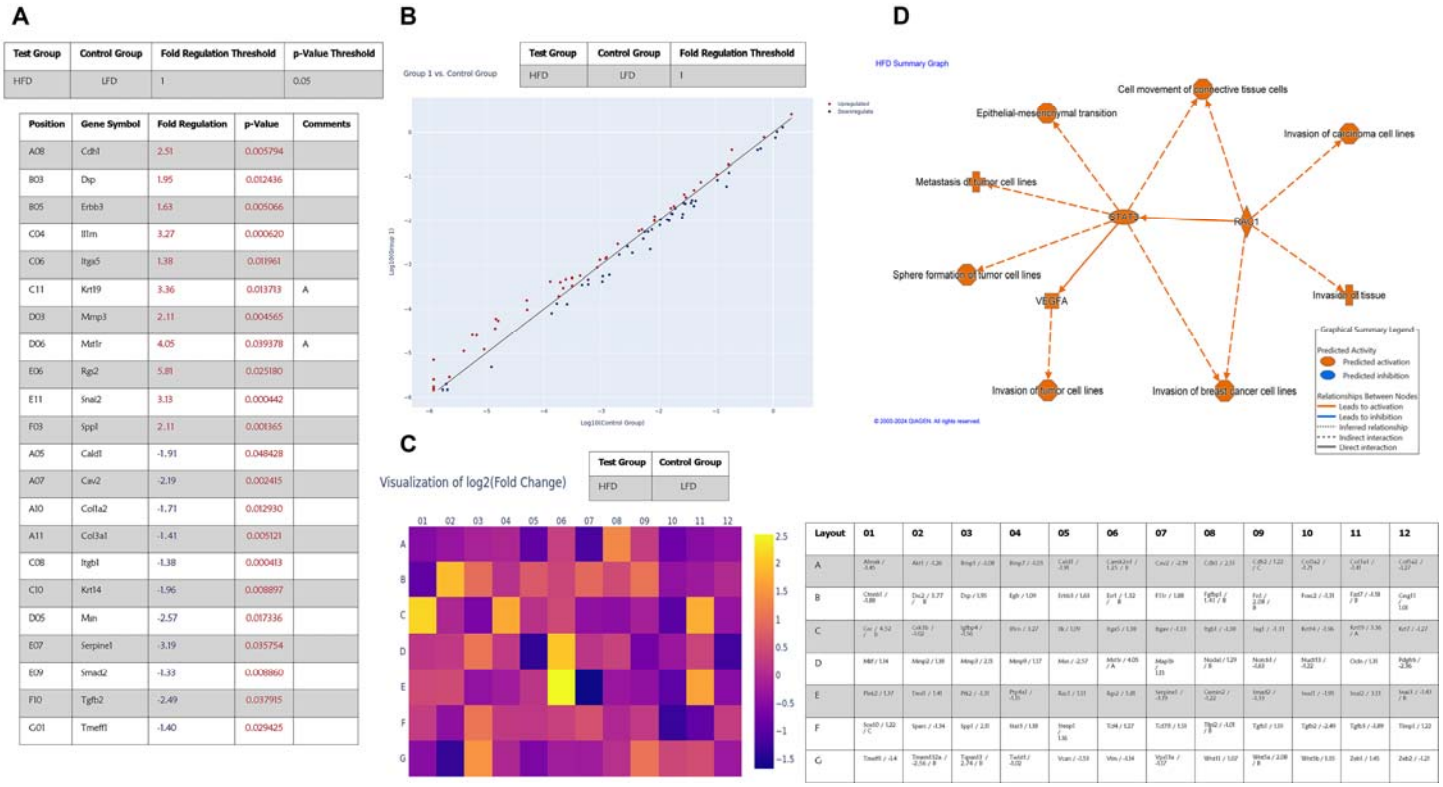

Test Group	Control Group	Fold Regulation Threshold	p-Value Threshold
HFD	LFD	1	0.05

Position	Gene Symbol	Fold Regulation	p-Value	Comments
A08	Cdh1	2.51	0.005794	
B03	Dsp	1.95	0.012436	
B05	Erbb3	1.63	0.005066	
C04	Il1rn	3.27	0.000620	
C06	Itga5	1.38	0.011961	
C11	Krt19	3.36	0.013713	A
D03	Mmp3	2.11	0.004565	
D06	Mst1r	4.05	0.039378	A
E06	Rgs2	5.81	0.025180	
E11	Snai2	3.13	0.000442	
F03	Spp1	2.11	0.008365	
A05	Cald1	-1.91	0.048428	
A07	Cav2	-2.19	0.002415	
A10	Col1a2	-1.71	0.012930	
A11	Col3a1	-1.41	0.005121	
C08	Itgb1	-1.38	0.000413	
C10	Krt14	-1.96	0.008897	
D05	Man	-2.57	0.017336	
E07	Serpine1	-3.19	0.035754	
E09	Smad2	-1.33	0.008860	
F10	Tgfb2	-2.49	0.037915	
G01	Tmeff1	-1.40	0.029425	

Test Group	Control Group	Fold Regulation Threshold
HFD	LFD	1

Test Group	Control Group
HFD	LFD

Layout	01	02	03	04	05	06	07	08	09	10	11	12
A	Ahnak / -1.45	Akt1 / -1.26	Bmp1 / -1.08	Bmp7 / -1.15	Cadherin / -1.38	Cameo2nd / 1.25 / B	Cav2 / -2.19	Cdh1 / 2.51	Cdh2 / 1.22 / C	Cd9a2 / -1.71	Col1a1 / -1.41	Col3a1 / -1.27
B	Ctnnb1 / -1.88	Dsc2 / 1.77 / B	Dsp / 1.95	Egfr / 1.09	Erbb3 / 1.63	Esr1 / 1.32 / B	Fn1r / 1.88	Fgfbp1 / 1.51 / B	Fzd / 1.08 / B	Fosl2 / -1.31	Fgf7 / -1.18 / B	Gngt1 / 1.01
C	Gsn / 4.52 / B	Cd170 / -1.02	Igfbp4 / -1.56	Il1rn / 3.27	Il6 / 1.29	Itga5 / 1.38	Itgav / -1.15	Itgb1 / -1.38	Itgl / -1.31	Krt14 / -1.96	Krt19 / 3.36 / A	Krt7 / -1.21
D	Mif / 1.14	Mmp2 / 1.38	Mmp3 / 2.11	Mmp9 / 1.17	Mse / -2.57	Mst1r / 4.05 / A	Map3k 1.21	Nodal / 1.29 / B	Notch1 / -1.03	Nudt13 / -1.22	Ocln / 1.31	Pdgfrb / -2.36
E	Plau2 / 1.37	Tnnt1 / 1.41	Pik2 / -1.31	Prp4k1 / -1.31	Rac1 / 1.11	Rgs2 / 5.81	Serpine1 / -3.19	Cxcrn2 / -1.22	Smad2 / -1.33	Snai2 / -1.95	Snai2 / 3.13	Snai3 / -1.43 / B
F	Sos10 / 1.20 / C	Spam / -1.34	Spp1 / 2.11	Stat3 / 1.18	Stmp1 / 1.16	Tcf4 / 1.27	Tcf19 / 1.19	Tfap2 / -1.03 / B	Tgfb1 / 1.19	Tgfb2 / -2.49	Tgfb3 / -1.89	Timp1 / 1.23
G	Tmeff1 / -1.4	Tmem52a / -2.56 / B	Tpm4l1 / 2.74 / B	Twist1 / -1.02	Vcan / -1.53	Vim / -1.34	Vnn1a / -1.17	Wnt11 / 1.17	Wnt5a / 2.08 / B	Wnt5b / 1.31	Zeb1 / 1.45	Zeb2 / -1.21

Supplementary Figure S3: EMT array gene expression and upregulated pathways in HFD plasma-derived exosomes.

(A) Fold regulation gene expression of E0771 significantly differentially regulated genes in HFD v.s. LFD plasma derived exosomes. (B) Scatter plot of HFD v.s. LFD plasma-derived exosomes. (C) Visualization of log2 (fold change) gene expression as a heatmap comparing HFD v.s. LFD. (D) IPA condensed graphical summary of activated pathways and functions in E0771 cells HFD-treated compared to LFD-treated. Gene expression plots were generated by Qiagen RT2 profiler online software. A p-value <0.05 and fold regulation >1 or <-1 was considered for gene expression analysis and significant. For pathway analysis, a z-score >2 or <-2 was considered as significant and included as an upregulated or downregulated pathways respectively.

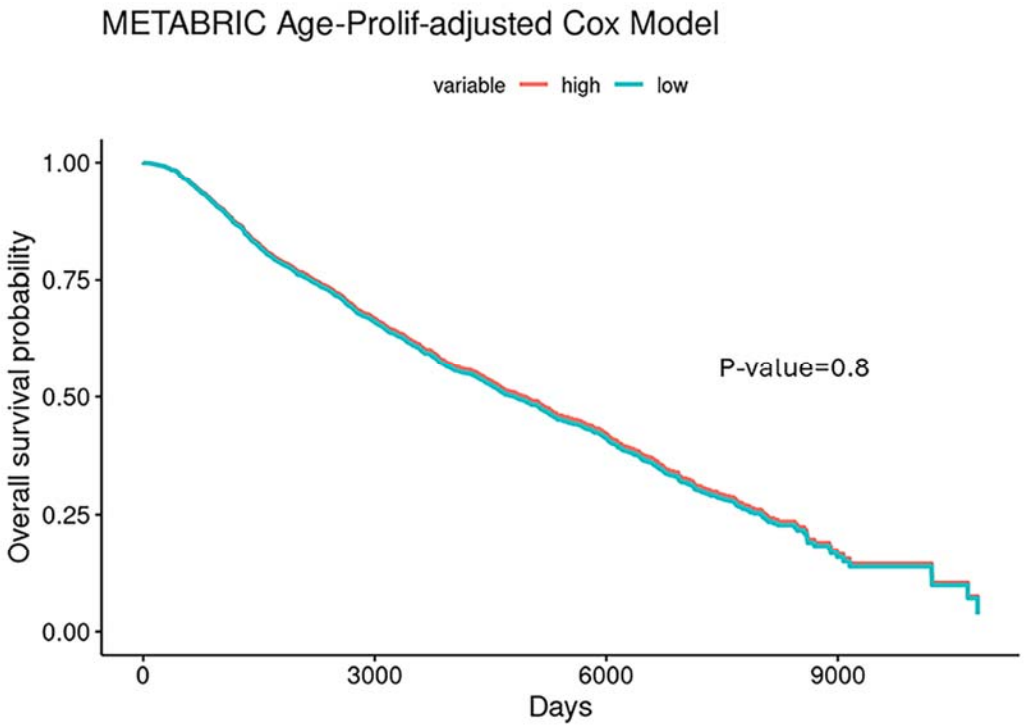

Supplementary Figure S4: METABRIC survival analysis of brain metastases in HFD/LFD plasma-derived exosomes treated E0771-GFP cells. Age and Proliferation Adjusted Survival curve based on the METABRIC cohort, illustrating overall survival probability for brain metastases in mice treated with HFD versus LFD-derived exosomes. No significant difference in survival was observed between the high and low expression groups (P-value = 0.8).

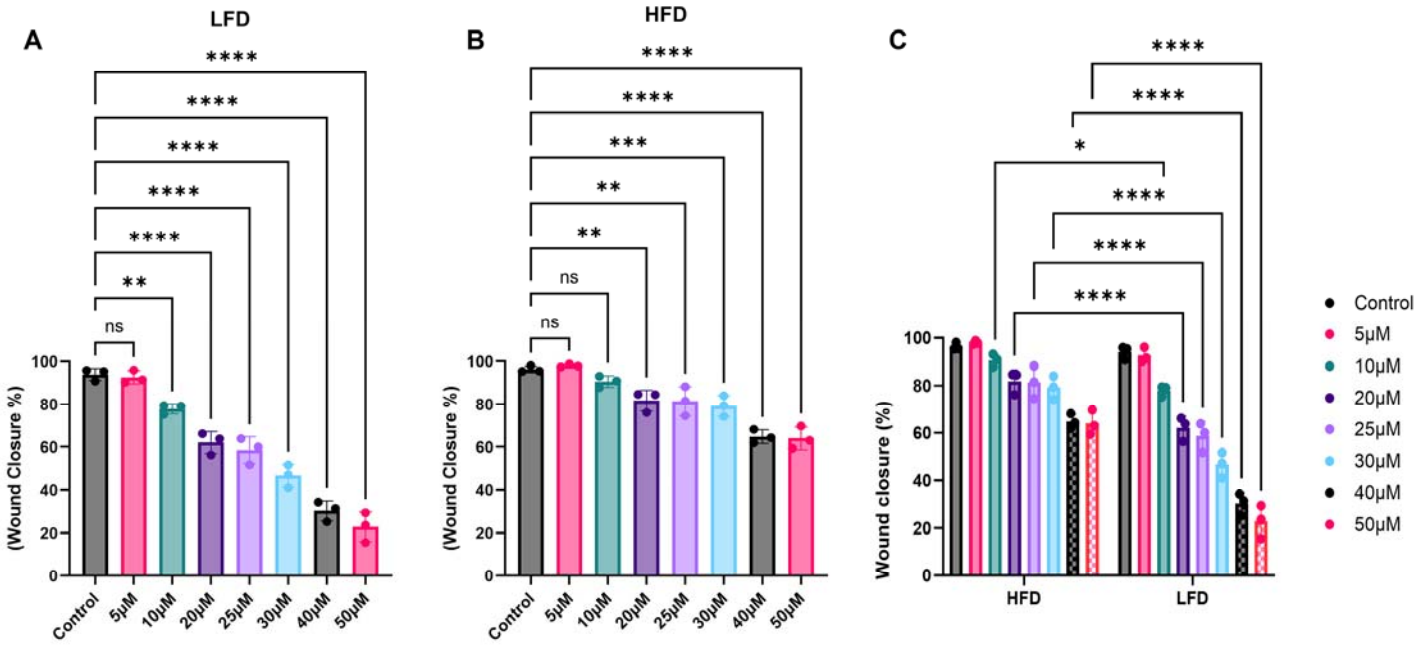

Supplementary Figure S5. Wound closure assay comparing the effects of EHT-1864 on HFD and LFD-plasma derived exosomes treated cells. Graph depicting the percentage of the wound that was closed after 24 hours across different concentrations of Rac1 inhibitor, EHT-1864 (5 µM, 10 µM, 20 µM, 25 µM, 30 µM, 40 µM, and 50 µM). (A) E0771 cells treated with LFD-plasma derived exosomes and (B) treated with HFD-plasma derived exosomes. In both HFD and LFD conditions, a dose-dependent reduction in wound closure was observed as the treatment concentration increased. HFD-treated cells had a less significant reduction in wound closure along the increasing concentrations of EHT-1864. (C) Comparison of wound closure across all concentrations in both HFD and LFD treatments. Wound closure was generally higher in LFD-treated cells at lower concentrations (5 µM and 10 µM), whereas HFD-treated cells exhibited significantly reduced closure rate at higher concentrations. Data were analyzed by 2way Anova with a Šidák's post-hoc analysis for multiple comparison testing with statistical significance presented as: ns, not significant, *$p < 0.05$; **$p < 0.01$; ***$p < 0.001$; ****$p < 0.0001$. N=3. All data are shown as mean ± SD.

Organ	Treatment	Biological Replicate	Colony Number (Count)	Area of Coverage (Size)	Cell count (Density)
Brain	HFD	1	148	0.092	219
		2	12	0.0128	42
		3	7	0.00929	20
		4	158	0.55	326
		5	22	0.0194	81
	LFD	1	0	0	0
		2	0	0	0
		3	6	0.0034	69
		4	6	0.011	37
		5	0	0	0
Lung	HFD	1	129	0.482	669
		2	94	0.0919	330
		3	80	0.343	210
		4	129	0.52	384
		5	100	0.386	380
	LFD	1	12	0.018	37
		2	3	0.0051	8
		3	87	0.122	420
		4	14	0.0192	54
		5	5	0.0122	24

Supplementary Table S1: Effects of HFD and LFD on Colony Formation in Brain and Lung Organs.

Table presents data from biological replicates of brain and lung tissues obtained from C57BL/6J mice injected with E0771-GFP cells pre-treated for 72 hours with either HFD or LFD-plasma derived exosomes. Colony formation, quantified by colony number, was significantly higher in HFD-treated brain and lung samples compared to their LFD counterparts. Specifically, the brain samples from HFD-treated subjects showed large colony counts, with a peak in replicate 4 (158 colonies), while LFD-treated brain replicates either exhibited no detectable colonies (replicates 1 and 2) or very low counts (6 colonies in replicates 3 and 4). Similarly, in lung tissues, replicates treated with an HFD consistently had higher colony numbers, with replicate 1 showing the maximum count (129 colonies), compared to much lower counts in LFD-treated lung replicates, with the highest colony count being only 87 (LFD biological replicate number 3).